

**Synthesis and Optical Properties of Colloidal BiI<sub>3</sub>  
Nanocrystals and Cs<sub>2</sub>AgBiBr<sub>6</sub>: analogues to Lead Halide  
Perovskite**

*A thesis submitted to*

**Indian Institute of Science Education and Research, Pune:**

for partial fulfilment of

BS-MS dual degree programme.



By

**Ashutosh Acharya (20121103)**

under the supervision of

**Dr. Angshuman Nag**

**Assistant Professor, Department of Chemistry**

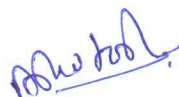
**Indian Institute of Science Education and Research, Pune**

## Certificate

This is to certify that this dissertation entitled "Synthesis and Optical Properties of Colloidal  $\text{BiI}_3$  Nanocrystals and Bulk  $\text{Cs}_2\text{AgBiBr}_6$ : analogous to Lead Halide Perovskites" towards the partial fulfilment of the BS-MS dual degree programme at the Indian Institute of Science Education and Research, Pune represents the research carried out by Ashutosh Acharya at IISER Pune under the supervision of "Dr. Angshuman Nag, Assistant Professor, Department of chemistry, IISER Pune" during the academic year 2016-2017.

Date: 20/3/2017

Place: Pune

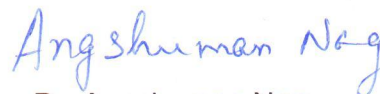


Ashutosh Acharya

5<sup>th</sup> year student

BS-MS dual degree

IISER Pune



Dr. Angshuman Nag

Assistant Professor

Department of chemistry

IISER Pune

## Declaration

I hereby declare that the matter embodied in the report entitled "Synthesis and Optical Properties of Colloidal  $\text{BiI}_3$  Nanocrystals and Bulk  $\text{Cs}_2\text{AgBiBr}_6$ : analogous to Lead Halide Perovskites" are the results of the investigations carried out by me at the Department of Chemistry, IISER Pune under the supervision of Dr. Angshuman Nag and the same has not been submitted elsewhere for any other degree.

Date: 20/3/2017

Place: Pune

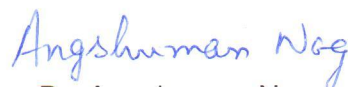


Ashutosh Acharya

5<sup>th</sup> year student

BS-MS dual degree

IISER Pune



Dr. Angshuman Nag

Assistant Professor

Department of chemistry

IISER Pune

# Acknowledgements

At first, I would like to express my deepest gratitude to my guide, Dr. **Angshuman Nag**, IISER Pune for providing me an incredible opportunity to carry out my 5th year MS thesis project under his guidance. His knowledge, aspirations, care, diligence and optimism, inspired me to work hard and expand my potential. I am thankful to my TAC member **Dr. Pramod Pillai**, Assistant Professor, Department of Chemistry, IISER Pune for his time and guidance throughout the project.

I would like to thank Jagdeesh and Gayatri for helping me in PL measurements, Shiva and Kavya for helping me in solid state measurements, Angha for helping me in FTIR measurements, Vikash for helping me in NMR analysis. I would also like to acknowledge Dr. JK and his group for providing me TGA measurement data.

I would like to thank my lab mate Bharat for helping me throughout my project and things without him would have been more depressing. I would like to thank my family members for being with me throughout. I am also thankful to my room-mate Harsh Jog and the BS-MS 2012 batch people for making my IISER Pune journey memorable.

# Table of contents

Abstract.....	1
1. Introductio.....	2
2. Chapter-1: BiI <sub>3</sub> Nanocrystals.....	6
2.1 Introduction.....	6
2.1.1 Crystal and electronic structure.....	6
2.1.2 Literature survey on solution processible BiI <sub>3</sub> NCs and current strategy	
2.2 Methodology.....	8
2.2.1 Chemicals.....	8
2.2.2 Synthesis.....	9
2.2.2.1 Bi-precursor preparation.....	9
2.2.2.2 I-precursor preparation.....	9
2.2.2.3 BiI <sub>3</sub> NCs preparation.....	9
2.2.3 Experimental characterization.....	9
2.2.4 No. of atoms in NC.....	10
2.2.5 Bohr excitonic diameter.....	10
2.2.6 PL quantum yield (PLQY).....	11
2.3 Results and Discussion.....	11
2.3.1 Structure and elemental analysis.....	11
2.3.2 Thermal analysis.....	13
2.3.3 Optical characterization.....	14
2.3.4 Surface characterization.....	18
2.3.5 MALDI-TOF analysis.....	21
2.4 Negative Results.....	22
2.4.1 BiI <sub>3</sub> NCs using different synthesis scheme.....	22
2.4.2 Bi <sub>2</sub> O <sub>3</sub> NCs.....	23
2.4.3 Bi NCs.....	24
2.5 Conclusions.....	25
3. Chapter-2: Bulk Cs <sub>2</sub> AgBiBr <sub>6</sub> Double Perovskite.....	26
3.1 Introduction.....	26

3.1.1	Crystal structure.....	26
3.2	Methodology.....	27
3.2.1	Chemicals.....	27
3.2.2	Preparation.....	27
3.3	Results and Discussion.....	28
3.3.1	Structural, morphological and elemental analysis.....	28
3.3.2	Optical characterization.....	29
3.4	Conclusions.....	30
4.	References.....	31

## List of figures

1. Previously reported CsPbX <sub>3</sub> NCs.....	3
2. Schematic representation of molecular orbital structure of CdS and CsPbX <sub>3</sub> ....	4
3. Crystal and electronic structure of BiI <sub>3</sub> .....	7
4. Structural and elemental analysis of BiI <sub>3</sub> NCs.....	12
5. Thermal analysis of BiI <sub>3</sub> NCs.....	13
6. Optical characterization of BiI <sub>3</sub> NCs.....	15
7. Schematic of band structure of direct and indirect semiconductor.....	17
8. <sup>1</sup> H NMR spectrum of BiI <sub>3</sub> NCs (C <sub>6</sub> D <sub>6</sub> ), oleylamine and 1-octadecene.....	19
9. 2D-DOSY (C <sub>6</sub> D <sub>6</sub> ) and FTIR spectrum of BiI <sub>3</sub> NCs.....	20
10. MALDI-TOF spectrum of BiI <sub>3</sub> NCs.....	21
11. Characterization of BiI <sub>3</sub> NCs.....	22
12. Characterization of Bi <sub>2</sub> O <sub>3</sub> NCs.....	23
13. Characterization of Bi NCs.....	24
14. Crystal structure of Cs <sub>2</sub> AgBiBr <sub>6</sub> .....	27
15. Structural, morphological and elemental analysis of Cs <sub>2</sub> AgBiBr <sub>6</sub> .....	29
16. Optical Characterization of Cs <sub>2</sub> AgBiBr <sub>6</sub> .....	30

## List of tables

1. Table 1: Previous strategies to synthesize solution processible BiI <sub>3</sub> NCs.....	8
2. Table 2: Formula obtained from the MALDI-TOF.....	21

## Abstract

Current research interest in nano material based optoelectronics is dominated by colloidal lead halide perovskites nanocrystals (NCs) because of their defect tolerant nature. This defect tolerant nature is a consequence of its unique electronic band structure where both valence band maximum and conduction band minimum possess an antibonding character along with the desired crystal structure. Interestingly, due to analogous electronic configuration,  $\text{Bi}^{3+}$  halides also adopt a similar electronic structure though a different crystal structure and are therefore expected to yield similar exciting properties. Motivated by this similarity, we investigated optical properties of solution processed  $\text{BiI}_3$  NCs to test its potential as lead free defect tolerant material.

$\text{BiI}_3$  NCs with a band-gap of 3.2 eV spanning in the near UV-region, emitted room-temperature band-edge photoluminescence (PL) in the blue region of visible spectrum with PL quantum yield (PLQY)  $\sim$  14%. Bi-exponential PL decay was obtained for  $\text{BiI}_3$  NCs with radiative recombination lifetimes of 2.4 ns and 5.6 ns. NMR, 2D-DOSY and FTIR confirmed that  $\text{BiI}_3$  NCs remain dispersed in solution through oleylamine passivation.  $\text{BiI}_3$  NCs demonstrate great potential for light emitting diodes and radiation detector owing to their low toxicity, favourable PLQY in blue/violet spectral region. Such a high PL efficiency for high band gap material ( $>2.5$  eV), suggests the defect tolerant nature of our  $\text{BiI}_3$  NCs.

Crystal structure of lead halide perovskite also adds to its defect tolerant nature. Double perovskite  $\text{Cs}_2\text{AgBiBr}_6$  have crystal structure similar to lead halide perovskite. Bulk  $\text{Cs}_2\text{AgBiBr}_6$  has been synthesized via solution processible method. X-ray diffraction pattern and elemental analysis confirmed the formation of cubic double perovskite structure with many different morphology. Diffuse reflectance measurements reveal band gap of 2.3 eV and that is comparable to analogous lead halide perovskite,  $\text{CsPbBr}_3$  (2.4 eV).  $\text{Cs}_2\text{AgBiBr}_6$  remains stable in environmental condition for at least 20 days with further study in progress. In future we aim to synthesis colloidal double perovskite NCs. These results suggest that Bi based halides can probably act as replacement of lead based perovskite.



## 1. Introduction

Most optoelectronic devices now days are fabricated employing highly crystalline Si and GaAs wafers. However, high manufacturing costs have proved to be a continuous obstacle in their mass commercialization and scientific community is eagerly searching for better and cost effective alternatives to these materials. In this aspect, colloidal semiconductor (SC) nanocrystals (NCs) have become extremely popular in last three decades because they can display tunable band gaps owing to quantum confinement effect and are solution processable. However, even after numerous attempts, the efficiency of the devices fabricated using SC NCs is way less than those finished using Si or GaAs. One of the primary reasons behind their failure is localized trap states or defect states in the mid-gap region between valence band maximum (VBM) and conduction band minimum (CBM) and such trap typically arise from non-bonded dangling bonds present on the surface of NC.

Therefore, researchers are now trying to manipulate VBM and CBM levels such that defect states present in between band gap region do not affect the optical process. First success in this direction was achieved when researchers discovered defect tolerant lead halide perovskite NCs. Since that discovery, the potential of perovskite materials in optoelectronics has been explored extensively and enormous success has been achieved. For example, Protesescu et al<sup>1</sup> showed near unity photoluminescence (PL) efficiency from colloidal CsPbX<sub>3</sub> (X= Cl, Br, I) NCs along with tunability throughout the visible range. Figure 1a,b represent such intense luminescence from CsPbX<sub>3</sub> NCs solution, where tunable emission in the visible region was achieved by changing the halide compositions. Yettapu et al<sup>2</sup> used terahertz (THz) spectroscopy establishing long-lived carriers in ~11 nm CsPbX<sub>3</sub> NCs yielding high carrier mobility of ~ 4500 cm<sup>2</sup>V<sup>-1</sup>s<sup>-1</sup>, and large diffusion length of >9.2 μm (Figure 1c). Apart from these properties, lead based perovskites have also been explored as active materials in solar cell devices and solar cell efficiencies (~16%)<sup>3</sup> have been accomplished in almost no time.

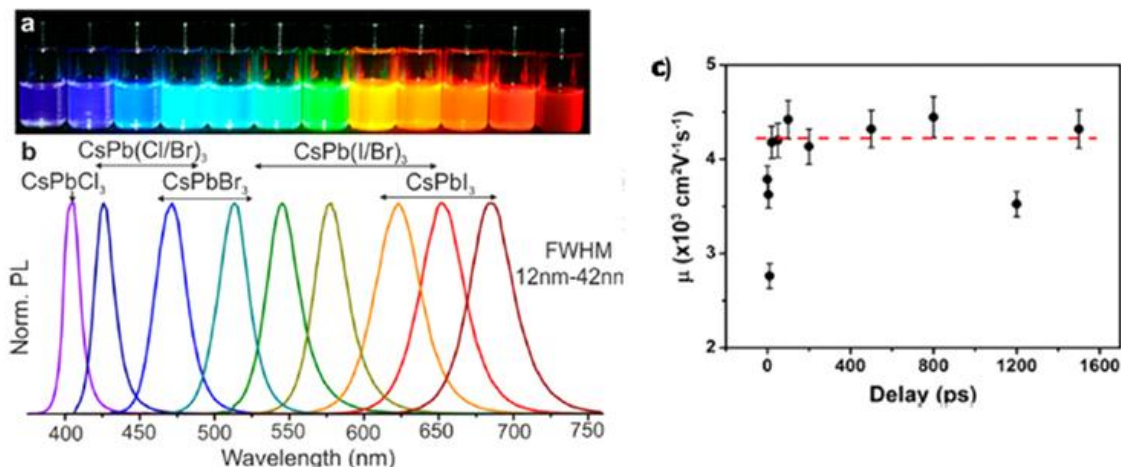


**Figure 1:** (a) Photograph of colloidal CsPbX<sub>3</sub> (X=Cl, Br, I) NCs dispersed in toluene under UV lamp. (b) PL spectra of respective samples shown in (a), (excitation wavelength: 400 nm except CsPbCl<sub>3</sub> where it is 340 nm). (c) Carrier mobility plotted with delay time obtained using THz spectroscopy. Carrier mobility is within the colloidal CsPBX<sub>3</sub> NC and delay time is time difference between pump laser arriving from optical pump and probe laser arriving from THz probe. Average mobility at 20 ps delay time is shown by red dashed line. (Figure reproduced from Protesescu et al<sup>1</sup> and figure 1c reproduced from Yettapu et al<sup>2</sup> after taking appropriate permissions from American Chemical Society.)

Theoretical calculations have suggested that probably the origin of these exciting properties in lead halide perovskite is its unique electronic band structure. To understand this, we compare the molecular orbital structure of CdS and CsPbX<sub>3</sub> perovskite in figure 2. In CdS, hybridization of Cd (5s) and S (3p) results into bonding and anti-bonding orbitals where bonding orbitals with filled levels constitute the VB and CB originating from empty anti-bonding orbitals. Since, the atomic states of Cd (5s) and S(3p) lie in between the VBM and CBM, any non-bonding state arising from them will contribute towards formation of trap states in the mid-gap region which kill the photo-excited electron. On the other hand, in CsPbX<sub>3</sub>, VBM originates from Pb (6s) and X (5p) anti-bonding interactions and CBM from Pb (6p) and X (5p) anti-bonding interactions. So probably non-bonding atomic states arising from Pb (6s) and X (5p) lie below the valence band and do not contribute in any kind of trap in between VBM and CBM or form the shallow defect states. Moreover, it has been proved theoretically that these

shallow states defect are delocalized in nature, and do not form efficient localized trap states.<sup>4</sup> Spin orbit coupling also helps via stabilizing CBM.

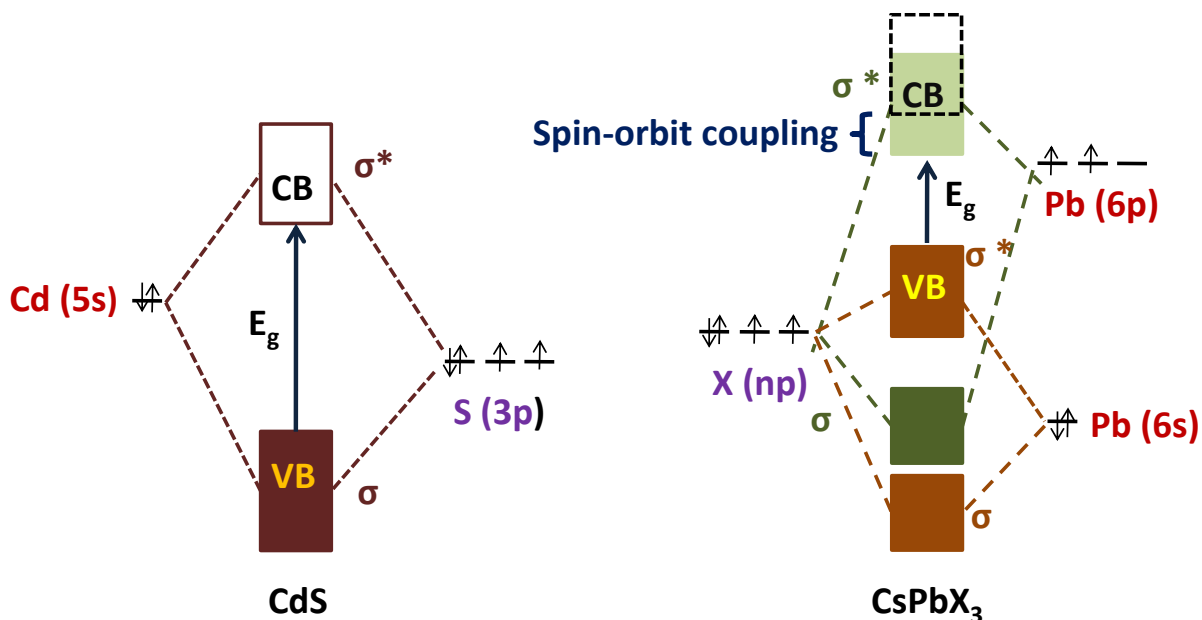


**Figure 2:** Schematic representation of bonding ( $\sigma$ ) and anti-bonding ( $\sigma^*$ ) orbitals of CdS and CsPbX<sub>3</sub> (X = Cl, Br, I) showing the formation of the valence and conduction band. (CdS band structure adapted from Eriksson et al<sup>5</sup> report and CsPbX<sub>3</sub> band structure adapted from Yuan et al<sup>6</sup> report)

Furthermore, we know that organic capping helps in stabilization of NCs in colloidal dispersion. To understand whether these capping ligands can also form localized trap states in between VBM and CBM in CsPbX<sub>3</sub> NCs, Brinck et al<sup>7</sup> calculated the electronic band structure of methyl ammonium capped CsPbX<sub>3</sub> NCs which revealed that states originating from organic capping do not contribute towards localized trap states within the band gap.

Although, CsPbX<sub>3</sub> exhibit all these fascinating fundamental properties, but they suffer with drawbacks such as they degrade upon exposure to moisture, heat<sup>8</sup> and light.<sup>9</sup> They also have tendency of halide migration creating a vacancy that disrupt the structure.<sup>10</sup> Presence of toxic lead raises serious concerns about the potential environmental hazards of these materials.<sup>11</sup> Thus, identifying a stable, non-toxic, defect tolerant material is one of the key challenges to be addressed.

To address the above issues one of the possible approach is to discover stable metal-halide alternatives composed of elements with similar band structure as that of CsPbX<sub>3</sub>. Computational study<sup>12</sup> suggests that Sn<sup>2+</sup>, Tl<sup>+</sup> and Bi<sup>3+</sup> have similar ns<sup>2</sup> electronic configuration in their outermost orbital and their halides could potentially act as replacement of Pb<sup>2+</sup>. Unfortunately, Sn based perovskites are extremely unstable in air due to oxidation of Sn<sup>2+</sup> to Sn<sup>4+</sup> even when handled in an inert atmosphere.<sup>13</sup> Therefore, by looking at current research scenario, it is highly unlikely that the Sn halide perovskites will ever have stability to replace Pb halide perovskites from devices. Tl, on the other hand is equally toxic as Pb. However, colloidal BiX<sub>3</sub> NCs are completely unexplored in literature and could be an exciting candidate for this purpose. It does not have stability concerns like Sn<sup>2+</sup>, due to stable +3 oxidation state and is non-toxic in all forms. This motivated us to synthesize and explore the photo-physical properties of BiI<sub>3</sub> NCs and is discussed in detail in chapter-1.

Another route is to look for a combination of ionic charges similar to perovskites such as A<sup>2+</sup>M<sup>2+</sup>X<sub>3</sub>, while maintaining the crystal structure and charge neutrality. Many possible combinations have been discovered but unfortunately none of them could accomplish the exciting properties as those in Pb-halide perovskites.<sup>14</sup> Therefore, some groups proposed to move to a quaternary A<sup>2+</sup>M<sup>+</sup>M<sup>3+</sup>X<sub>6</sub> system, i.e. double perovskites.<sup>15</sup> There are certain ions such as Cu<sup>+</sup>, Ag<sup>+</sup>, Bi<sup>3+</sup>, Sb<sup>3+</sup> that possess analogous atomistic behaviour to Pb<sup>2+</sup> and their combinations can perhaps result in stable double perovskites with efficient optoelectronic properties. Here we aim to synthesize Cs<sub>2</sub>AgBiBr<sub>6</sub> in bulk and nano regime and do their optoelectronic studies. However, till now we were able to synthesize bulk part and is discussed in detail in chapter 2. This chapter only reproduces data that was previously reported by Eric et al.<sup>15b</sup>

## Chapter: 1

### Bil<sub>3</sub> NCs

#### 2.1 Introduction

Bismuth triiodide (BiI<sub>3</sub>) belongs to family of layered metal semiconductors. Thin films and single crystals of BiI<sub>3</sub> have been investigated as hard radiation detector<sup>16</sup> and for X-ray imaging<sup>17</sup> due to their relatively high resistivity up to 10<sup>9</sup> Ω-cm<sup>17b, 18</sup>, large static dielectric constant<sup>19</sup>, high density and high atomic numbers of the constituent elements. BiI<sub>3</sub> has an indirect band gap of 1.8 eV and direct band gap of 2.0 eV.<sup>20</sup> Calculated hole and electron effective masses are 10.3 m<sub>0</sub> and 1.8 m<sub>0</sub>, respectively.<sup>12</sup>. Because of higher effective hole mass, its hole mobility is expected to be very less compared to electron mobility. Electron mobility of 260 ± 50 cm<sup>2</sup>/(V·s) has been obtained in BiI<sub>3</sub>, which though not the best but is definitely encouraging for additional exploration.<sup>17b, 18</sup> BiI<sub>3</sub> was also investigated as electron transport layer (ETL) in solar cells with poly-triarylamine as hole transport layer (HTL) and power conversion efficiency (PCE) and external quantum efficiency (EQE) of solar cell were found to be 0.32% and 20%, respectively.<sup>21</sup>

##### 2.1.1 Crystal and electronic structure

BiI<sub>3</sub> crystallizes in a rhombohedral crystal structure (space group R $\bar{3}$ , No. 148) with six formula units per unit cell where bond between Bi and I is ionic in nature with bond length 3.1 Å. A schematic representation of the BiI<sub>3</sub> crystal structure is shown in figure 3a,b. The lattice parameters of BiI<sub>3</sub> are a 8.13 Å and  $\alpha = 56.17^\circ$ .<sup>18</sup> Within the lattice, Bi<sup>3+</sup> ions occupy the 6c Wyckoff positions with coordinates (0, 0, 0.16), while the I<sup>-</sup> ions reside in the 18f positions with coordinates (0.33, 0.31, 0.07).<sup>22</sup> It can also be seen from the crystal structure that BiI<sub>3</sub> adopts a layered structure with Bi<sup>3+</sup> ions adopting a six-fold coordination with I<sup>-</sup> ions. Bismuth occupies only two third of octahedral voids. Layers separated by distance of 3.78 Å are held together with weak vander waal interactions<sup>23</sup>

and therefore slight perturbation by external factors such as strain, stress can easily produce disorders in the layers.<sup>24</sup>

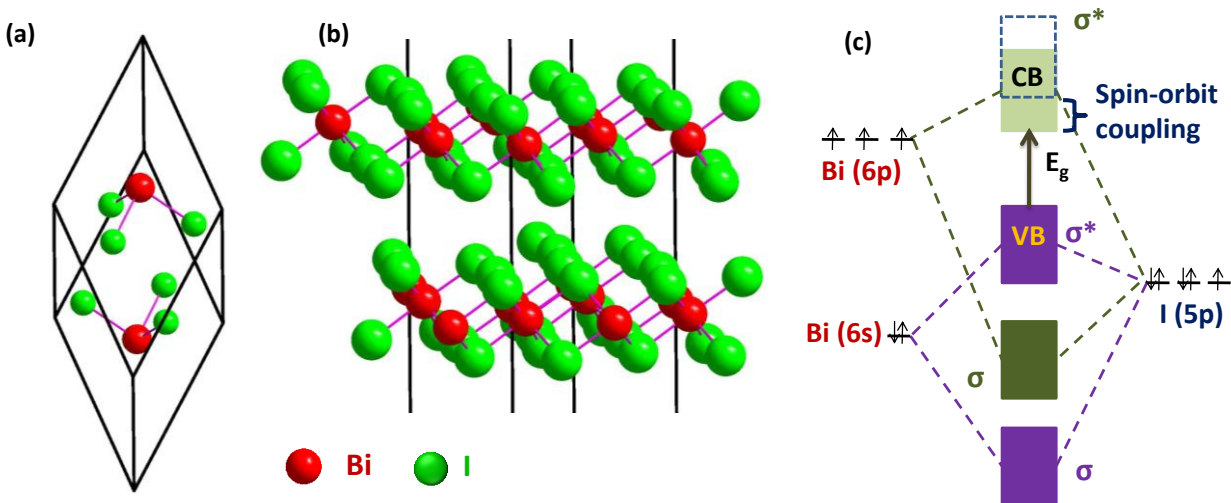


**Figure 3:** Crystal structure and electronic structure of BiI<sub>3</sub>. (a) Rhombohedral unit cell of BiI<sub>3</sub> crystal. (b) Layered structure showing octahedral coordination of Bi. (c) Schematic representation of molecular orbital structure of BiI<sub>3</sub> showing the valence band and conduction band are made of anti-bonding orbital and trap states lie below valence band. (molecular orbital structure of BiI<sub>3</sub> is adapted from Brandt et al<sup>25</sup>)

Figure 3c shows schematic of molecular orbital structure of BiI<sub>3</sub>. The molecular orbital structure of BiI<sub>3</sub> is similar to Pb based perovskites as Bi<sup>3+</sup> also consists inert 6s<sup>2</sup> lone pair of electrons as Pb<sup>2+</sup>. Anti-bonding interaction of inert 6s<sup>2</sup> lone pair of electron of Bi<sup>3+</sup> with 5p orbital of I<sup>-</sup> forms VBM and 6p orbital of Bi contribute in the formation of CBM. Further, Similar to CsPbX<sub>3</sub> perovskite BiI<sub>3</sub> also shows spin-orbit coupling which stabilizes its CBM.

### 2.1.2 Literature survey on solution processible BiI<sub>3</sub> NCs and current strategy

There are few reports on synthesis and characterization of BiI<sub>3</sub> NCs. Table 1 shows the comparison of the previously synthesized solution processible BiI<sub>3</sub> NCs. Apart from Fornero et al<sup>26</sup> all the synthesis were carried out at room temperature in polar solvent with no capping ligand. Apart from Micic et al<sup>27</sup> who also achieved very weak PL, no one could achieve PL. We believe that absence of PL in previously synthesized BiI<sub>3</sub> NCs is possibly due to either absence of ligands or lower reaction temperature or both. Surface

ligands have direct influence on the optical, electrical, catalytic and magnetic properties of NCs. If capping ligands are present on the NCs surface then bonding between the ligand orbitals and NC surface atom might shift defect states outside the band gap removing the trap states. DFT calculation also agrees that in certain ligand capped NCs mid-gap trap states disappear.<sup>28</sup> It has been also found that in CdSe NCs loss of surface ligands during dilution and purification leads to decrease in PL intensity.<sup>29</sup>

**Table 1:** Previous strategies to synthesize solution processible BiI<sub>3</sub> NCs

Ref.	Bismuth and Iodine precursors		Solvent	Reaction Temp.(°C)	Size (nm)	E <sub>g</sub> (eV)	PL
27	BiCl <sub>3</sub>	KI	CH <sub>3</sub> CN	25	-	3.1	Weak
30	Bi(NO <sub>3</sub> ) <sub>3</sub> .5H <sub>2</sub> O	KI	H <sub>2</sub> O	25	2-8	2.6, 3.2	No
26	Bi(NO <sub>3</sub> ) <sub>3</sub> .5H <sub>2</sub> O	KI + I <sub>2</sub>	1-Octadecene	180-200	80-140	-	No
31	Bi(NO <sub>3</sub> ) <sub>3</sub> .5H <sub>2</sub> O	KI	H <sub>2</sub> O	25	1.6, 3.4	3.2	No
32	BiI <sub>3</sub>	-	Isopropanol	25	8	2.7	No

Temperature plays a crucial role in determining the crystallinity of NCs. Increasing the synthesis temperature offers enhanced probability of the exclusion of defects from NC due to self-purification mechanism during growth of NCs. As a result of this, high temperature synthesis of nanomaterials is often accompanied with high crystallinity and superior PL efficiencies.

So keeping in mind the effect of capping ligands and reaction temperature on NCs growth we prepared oleylamine capped BiI<sub>3</sub> NCs employing 240 °C reaction temperature.

## 2.2 Methodology

**2.2.1 Chemicals:** All the chemicals used are commercially available. Bismuth nitrate penta-hydrate (Bi(NO<sub>3</sub>)<sub>3</sub>.5H<sub>2</sub>O, purity ≥ 99.99%), Iodine (I<sub>2</sub>, purity ≥ 98%), 1-octadecene (purity ≥ tech. 90%), oleylamine (purity ≥ tech. 98%), potassium bromide (KBr, purity ≥ 99%) and Quinine sulphate dye (purity ≥ 98.5-100.5%), sulphuric acid (H<sub>2</sub>SO<sub>4</sub>, 48 %),

anhydrous chloroform (purity  $\geq 99.5\%$ ), dithranol, deuterated benzene( $C_6d_6$ ), Anhydrous Toluene (purity  $\geq 99.5\%$ ) were purchased from sigma-aldrich, ethanol (purity  $\geq 99.9\%$ ), was purchased from Rankem chemicals.

## 2.2.2 Synthesis

**2.2.2.1 Bi Precursor:** 0.25 mmol of  $Bi(NO_3)_3 \cdot 5H_2O$  and 12 mL oleylamine were taken in a three-necked round bottom flask and applied vacuum at 100 °C for about 1 hour. The temperature of reaction mixture was then raised to 240 °C under  $N_2$  atmosphere and kept there until solution becomes clear.

**2.2.2.2 Iodine Precursor:** Simultaneously, in another three-neck round bottom flask 10 mL 1-octadecene was taken and degassed at 100 °C for about 1 hour. The solution was then allowed to cool under  $N_2$  atmosphere. In another round bottom flask, 0.75 mmol  $I_2$  was taken and kept under  $N_2$  atmosphere. 10 ml 1-octadecene (already degassed) was injected in this and temperature was raised to 60 °C and kept there until solution becomes clear.

**2.2.2.3  $BiI_3$  NCs Preparation:** Iodine Precursor was immediately injected into Bi precursor at 240 °C and reaction was quenched immediately using dry ice in acetone and while cooling when temperature was 140 °C, 10 ml anhydrous toluene was injected. The obtained reaction product was centrifuged at 7000 rpm for 5 minute and the supernatant was taken up for further washing and precipitate was discarded. The NCs in supernatant were precipitated using little amounts of ethanol and dispersed in anhydrous toluene. Obtained dispersion was centrifuged at 3000 rpm for 2 minute and the supernatant was taken up for further studies.

## 2.2.3 Experimental Characterization

Transmission electron microscope (TEM) images were obtained on a UHR FEG-TEM electron microscope using a 200 kV electron source. Powder XRD (p-XRD) data were recorded on Bruker D8 Advance X-ray diffractometer equipped with  $Cu K\alpha$  (1.54 Å) radiation. Energy dispersive X-ray spectroscopy (EDS) was performed by using Zeiss Ultra Plus SEM instrument fitted with a EDS detector. UV-visible absorption spectra



were measured using Perkin Elmer Lambda-45 UV/vis spectrometer. PL spectra and PL decay dynamics studies were carried out on Edinburg FLS980 spectrophotometer. The PL decay dynamics were studied using 340 nm nanosecond pulse LED lasers as excitation source. All NMR experiments were carried out using a Bruker Avance III HD spectrometer operating at a 1 H frequency of 400 MHz, at 298K. 1 H, 2D NOESY and 2D DOSY were acquired using standard pulse sequences from the Bruker library. Fourier transform infrared spectroscopy (FTIR) studies were performed using NICOLET 6700 FTIR spectrometer by making a pellet of BiI<sub>3</sub> NCs powder in KBr host. MALDI-TOF spectrum was obtained on 4800 plus MALDI-TOF/TOF Analyser. PL quantum yield (PLQY) of BiI<sub>3</sub> NCs were obtained using quinine sulphate dye in 0.5 mol/L as reference (PLQY = 56%).

**2.2.4 No. of atoms in NC:** no. of atoms present in single unit cell = 2 Bi, 6 Iodine

$$\text{Volume of rhombohedral unit cell } (V_1) = a^3 (1 - 3\cos^2\alpha + 2\cos^3\alpha)^{1/2}$$

Here, a = lattice parameter of unit cell = 7.7 Å, and  $\alpha$ : angle between two sides = 56°

$$\text{Calculating, } V_1 = 0.3 \text{ nm}^3$$

$$\text{Volume of single spherical NC } (V_2) = 4/3 \pi r^3$$

Here, r: radius of NC = 2 nm

$$\text{Calculating, } V_2 = 4.1 \text{ nm}^3$$

$$\text{So, no. of unit cells in one NC} = V_2 / V_1 \sim 13$$

$$\text{So, no. of Bi atoms in single NC} = 2 \times 13 = 26 \text{ and no. of I in single NC} = 6 \times 13 = 78.$$

**2.2.5 Bohr excitonic diameter:**

$$\mathbf{a} = \text{Bohr excitonic diameter is given by } a = a_0 \epsilon_r / \mu_e^*$$

here,  $a_0$  : Bohr radius,  $\epsilon_r$  : dielectric constant of material,  $\mu_e^*$  : effective reduced mass of electron and hole.

$a_0$  : 0.53 Å,  $\mu_e^*$  : 0.63 and  $\epsilon_r$ : 54 and 8.6

Using, 1)  $\epsilon_r$ : 54 calculated Bohr excitonic diameter (a) = 4.3 nm

2)  $\epsilon_r$ : 8.6 calculated Bohr excitonic diameter (a) = 0.6 nm

**2.2.6 PL quantum yield (PLQY):** Reference method was used and the standard sample was quinine sulphate in 0.5 mol/L H<sub>2</sub>SO<sub>4</sub> under 340 nm source.

Formula:

$$\Phi_{\text{sample}} = \Phi_{\text{ref.}} \cdot \left\{ \frac{(I/A)_{\text{sample}} \cdot \eta_{\text{sample}}^2}{(I/A)_{\text{ref.}} \cdot \eta_{\text{ref.}}^2} \right\}$$

Herer,  $\Phi$  = quatum yield

$I/A$  = Area under the curve of absorbance normalized PL.

$\eta$  = refractive index

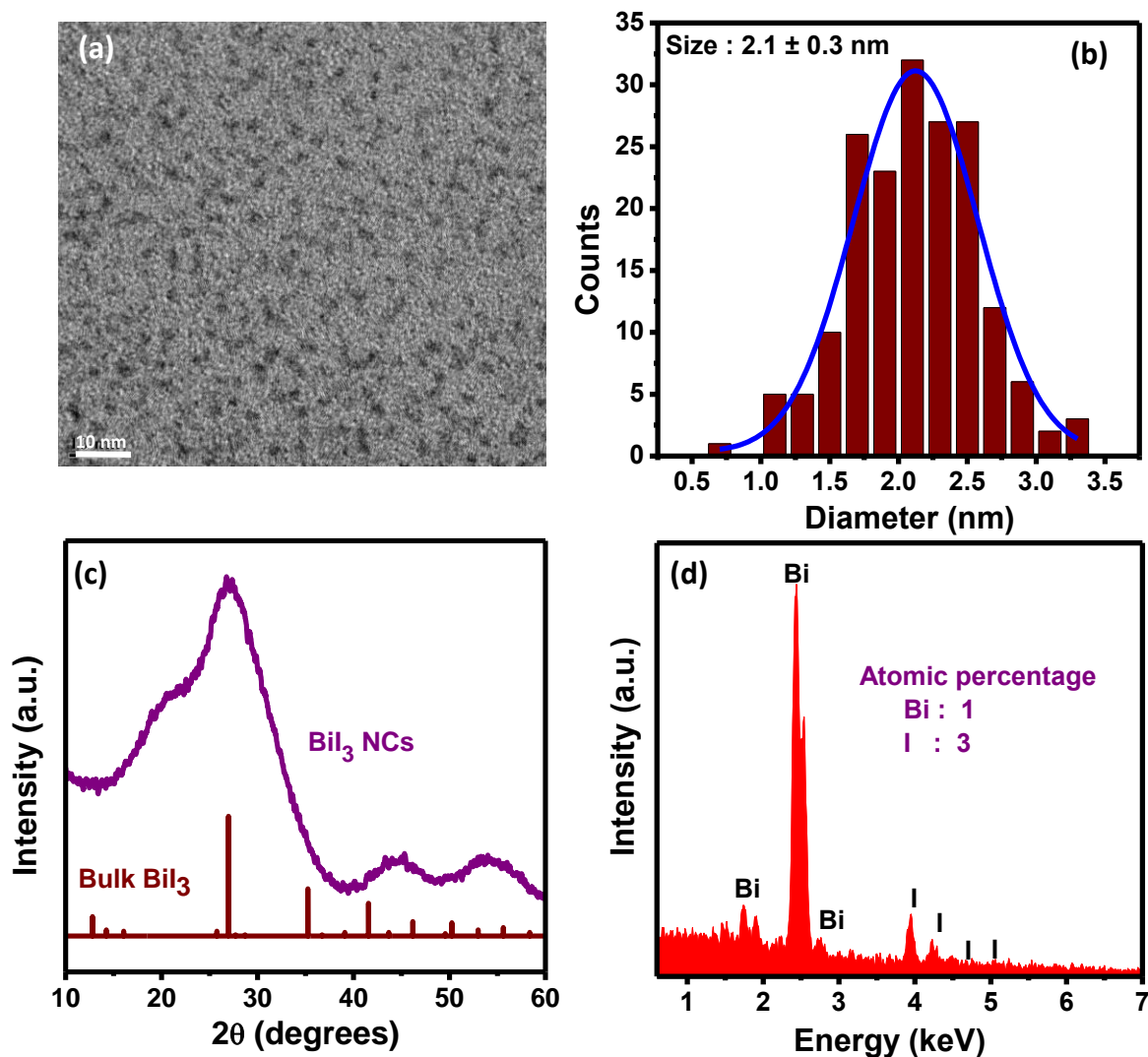
$\Phi_{\text{ref}} = 56\%$ ,  $I/A_{\text{sample}} = 1073268055.73$ ,  $I/A_{\text{ref.}} = 4826800059.8$ ,  $\eta_{\text{sample}} = 1.4$ , and  $\eta_{\text{ref.}} = 1.3$

Substituting values and calculating PLQY = 13.8% ~ 14%

## 2.3. Results and Discussion

### 2.3.1 Structure and elemental analysis

Figure 5a shows TEM Image of BiI<sub>3</sub> NCs. Size distribution histogram obtained from TEM image is shown figure 5b. The synthesized BiI<sub>3</sub> NCs have spherical morphology with an average diameter of 2.1 nm with a standard deviation of 0.3 nm. Reported values of dielectric constants are 54 ( $\epsilon_{||}$ ) and 8.6 ( $\epsilon_{\perp}$ ) for BiI<sub>3</sub>.<sup>19</sup> Calculated excitonic Bohr diameters (section 2.5) using these dielectric constant values were found to be 4.4 nm and 0.7 nm, respectively. The size of our NC is 2.1 nm and it is well below the Bohr excitonic diameter obtained from  $\epsilon_{||}$  value and well above the Bohr excitonic diameter obtained from  $\epsilon_{\perp}$  value.



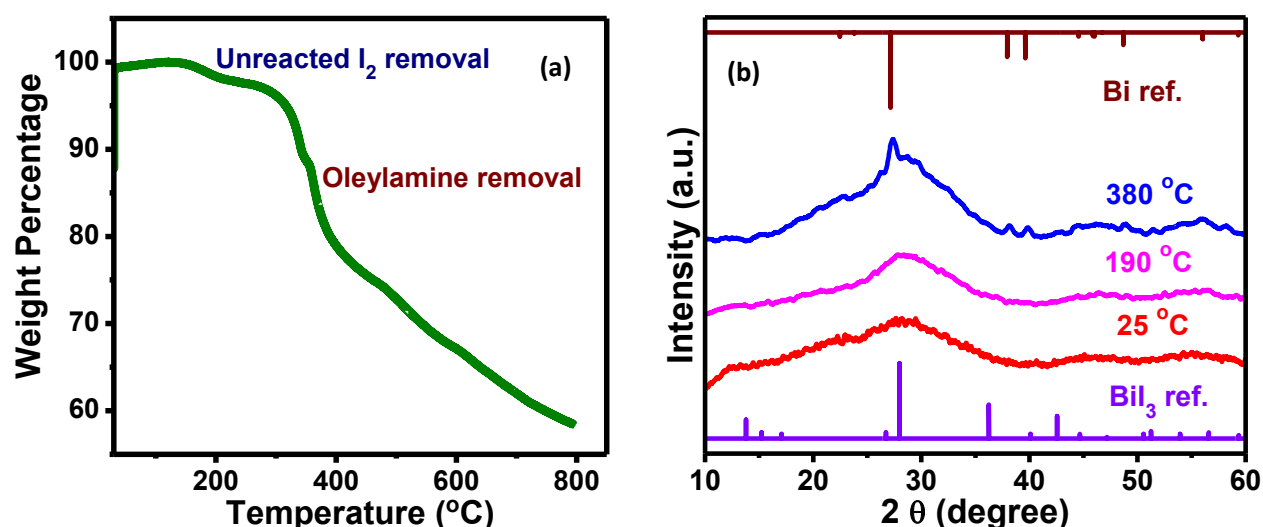
**Figure 4:** Structural, morphological and elemental characterization of BiI<sub>3</sub> NCs. (a) TEM image showing spherical morphology. (b) Histogram of size distribution obtained from TEM image. (c) p-XRD pattern of BiI<sub>3</sub> NCs plotted with bulk BiI<sub>3</sub>. (d) EDS spectrum showing elemental ratios of Bi and I is in 1:3.

Figure 5c shows the p-XRD spectrum of synthesized NCs. Presence of most intense peak (in agreement with bulk counterpart) in p-XRD suggests probable formation of crystalline BiI<sub>3</sub> NCs. In comparison with the bulk counter-part, the diffraction peaks are significantly broadened and all peaks are not present which is due to small size effect in NCs. The unit cell dimension for BiI<sub>3</sub> is 8.1 Å, with this lattice parameter, calculated

(section 2.4) number of Bi and I atoms in 2.1 nm sized NC is 28 and 78, respectively. With such a small number of atoms, constructive interference is not sufficient to produce the peaks with less intensity and we do not observe all peaks in p-XRD pattern. Consequently, the p-XRD pattern is insufficient to confirm the formation of  $\text{BiI}_3$  NCs.

EDS spectrum (figure 5d) shows presence of Bi and I in 1:3 ratio consistent with the formation of  $\text{BiI}_3$  NCs. On a different note, In EDS spectrum, we see that although Bi contributes less in atomic percentage but the peak intensity corresponding to that is very high compared to I. It is because absorption cross section of Bi is of the order of  $10^{25} \text{ cm}^2$  which is very high compare to I that is  $10^{-18} \text{ cm}^2$ . Higher absorption cross section guarantees more absorption hence higher intensity.<sup>33</sup>

### 2.3.2 Thermal analysis:



**Figure 5:** Thermal analysis. (a) Thermogravimetric analysis (TGA) NCs starts around 400 °C. (b) p-XRD of  $\text{BiI}_3$  NCs after heating at different temperature.

Further to check formation of  $\text{BiI}_3$ , TGA was performed. Figure 9a shows the thermogravimetric (TGA) spectrum of  $\text{BiI}_3$  NCs and figure 9b shows p-XRD of  $\text{BiI}_3$  powder after heating at different temperature. First we see 5% mass loss starting at 170°C up to 200 °C. This is due to loss of un-reacted  $\text{I}_2$  as boiling point of  $\text{I}_2$  is 184 °C. p-XRD confirms this as there is no change in p-XRD pattern obtained after heating at 190 °C compare to room temperature p-XRD pattern. Further there is mass loss of 20% between 320 °C to 400 °C. This weight loss is assigned to removal of organic capping

from NCs. There is appearance of Bi peaks in p-XRD pattern obtained after heating at 380 °C. This indicates that around 380 °C  $\text{BiI}_3$  start to dissociate into Bi metal. After that continuous weight loss is observed and this can be assigned to decomposition of  $\text{BiI}_3$  into Bi metal.<sup>25</sup> In literature it is already reported that above 400 °C  $\text{BiI}_3$  decomposes into Bi metal and we also observe the same, so this is an indirect evidence which confirms the formation of  $\text{BiI}_3$ . So together p-XRD, EDS and TGA confirms the formation of  $\text{BiI}_3$  NCs.

### 2.3.3 Optical characterization

Figure 5a shows UV-visible absorption, PL and photoluminescence excitation (PLE) spectrum of synthesized  $\text{BiI}_3$  NCs. In the absorption spectrum we observe a gradual increase in absorbance from 600nm to 500 nm and after that a sharp escalation. The solution appears colourless under white light (figure 5b) at room temperature, which signifies that it is not absorbing any light in visible region. Thus gradual rise from 600 nm to 500 nm is probably due to scattering and sharp escalation after that indicates band gap transition of  $\text{BiI}_3$  NCs. Absorption maximum is located at 380 nm (3.2 eV) and is significantly blue shifted compared to bulk band gap (2.1 eV). This blue shift signifies strong quantum confinement of charge carriers in our  $\text{BiI}_3$  NCs.  $\text{BiI}_3$  NCs exhibit room temperature PL. Emission maximum is observed at 410 nm and it is red shifted by of 30 nm (175 meV) compared to absorbance maximum. Such a meagre shift suggests excitonic emission corresponds to excitonic absorption. Figure 5c shows photograph of colloidal solution dispersed in anhydrous toluene under UV illumination (365 nm). Photoluminescence excitation (PLE) spectrum overlap with the absorption spectrum of  $\text{BiI}_3$  NCs confirms that PL is exhibited by  $\text{BiI}_3$  NCs.

The PLQY was calculated (section 2.6) using quinine sulphate reference dye dissolved in 0.5 mol/L  $\text{H}_2\text{SO}_4$ . Figure 5d shows the absorbance normalized PL intensity (relative PL intensity) of our NCs plotted with dye and by calculating area under the curve, reference PLQY obtained was ~14% for our  $\text{BiI}_3$  NCs. It has been already discussed that there are no prior literature reports showing PL from  $\text{BiI}_3$  NCs.

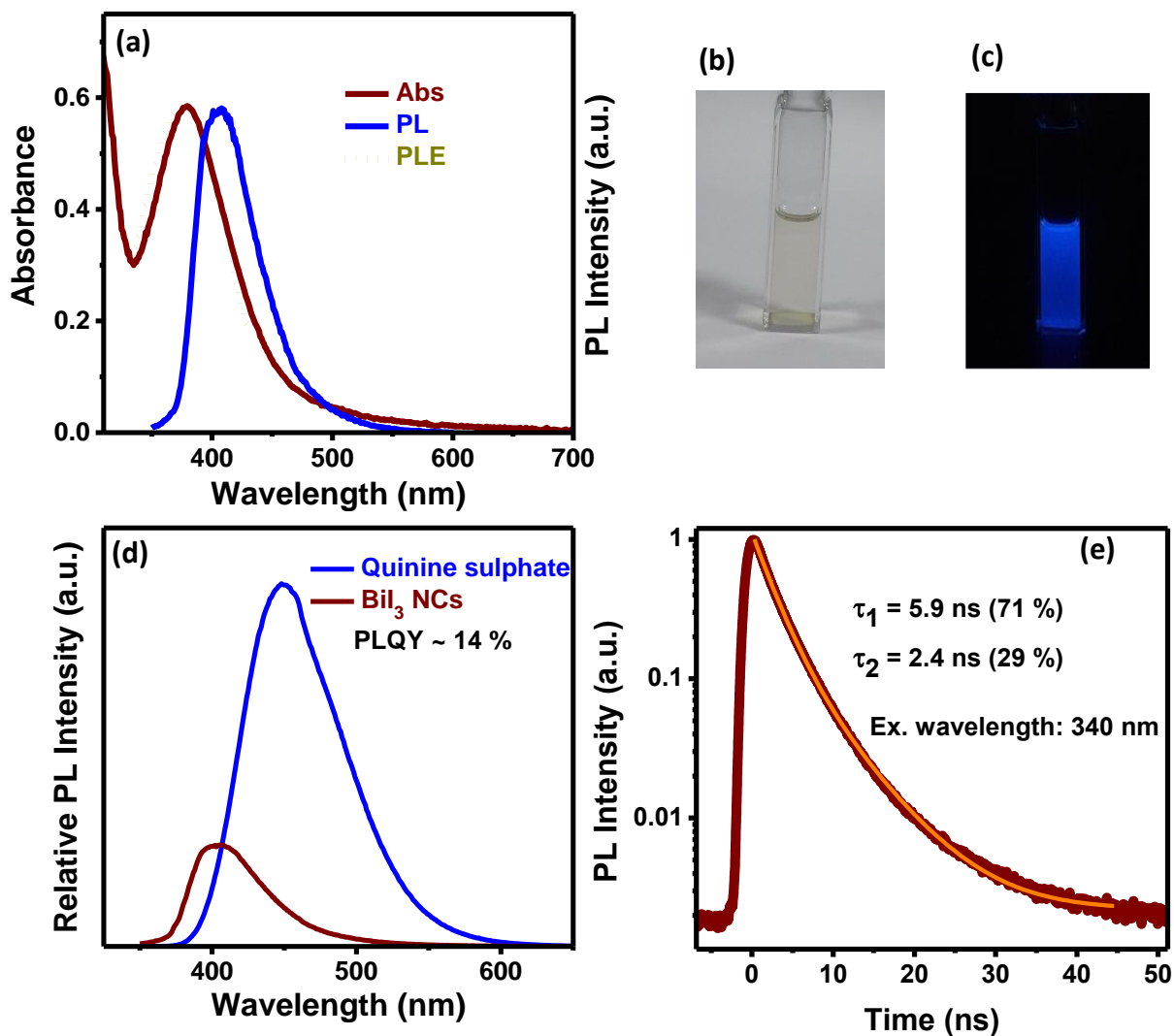


**Figure 6:** Optical characterization. (1) UV-visible absorption, PL and PLE spectra of BiI<sub>3</sub> NCs. (b), (c) Shows the photograph of BiI<sub>3</sub> NCs dispersed in toluene under white light and under UV light (365 nm wavelength), respectively. (d) PL spectrum of Quinine sulphate(QS) in 0.5 mol/L H<sub>2</sub>SO<sub>4</sub> plotted with BiI<sub>3</sub> NCs dispersed in toluene. (e) PL decay dynamics after excitation at 340 nm wavelength fitted with bi-exponential function showing lifetimes of 5.9 ns and 2.4 ns with contribution of 71% and 29%, respectively.

Probable reason behind PL from our NCs could be due to surface passivation by oleylamine which reduces the traps arising from dangling bonds reducing PL quenching. This is further assisted by higher temperature synthesis that enables good crystallinity and small size of our NCs. Smaller size enables increased overlap between electron

and hole wave functions, and would in turn enhance the transition probability between ground and excited state resulting into a PL for our  $\text{BiI}_3$  NCs at room temperature. Also, it should be noted that it is always challenging to obtain high PL efficiency in high band gap semiconductors, such as in CdS NCs due to high probability deep defect states by impurities. As a result PL quantum efficiency is usually quenched in presence of competing non-radiative pathways for these wide band gap semiconductors. In addition to defect states from dangling bonds and solvent, deformation in layers also contributes to defect states for our NCs.

To get further insight, PL decay dynamics were measured using TCSPC (time-correlated single photon counting) method. Figure 5e shows PL decay plots of colloidal  $\text{BiI}_3$  NCs at emission wavelength 410 nm after excitation at 340 nm. Fitting with bi-exponential decay function gives radiative lifetimes of  $\tau_1 \sim 5.9$  ns with 71 % contribution and  $\tau_2 \sim 2.4$  ns with 29 % contribution. We believe that probably  $\tau_1$  decay corresponds to emission from delocalized shallow defect states located near either CBM or VBM and  $\tau_2$  belongs to the emission from CBM. However, the difference between  $\tau_1$  and  $\tau_2$  is not very significant to reach any conclusion and further understanding is required. Absence of long ( $\sim 100$  ns) lifetimes shows the absence of deep-trap related radiative recombination in our NCs. Presence of sharp escalation in band gap, high PLQY in violet region and absence of long lifetimes indicates direct band gap nature of our  $\text{BiI}_3$  NCs.

Although our  $\text{BiI}_3$  NCs show direct band gap semiconductor nature but in bulk  $\text{BiI}_3$  is an indirect band gap semiconductor. As far our knowledge there are no prior literature reports that suggest that  $\text{BiI}_3$  is as direct band gap semiconductor in nano regime. So considering that aspect and assuming our  $\text{BiI}_3$  NCs as indirect band gap material here we try to explain possibility of achieving PL from an indirect band gap semiconductor. For any transition to occur momentum and energy has to be conserve. Figure 6 shows transition in direct and indirect band gap semiconductor. For direct band gap semiconductor due to same  $\mathbf{K}$  (momentum vector) value of VBM and CBM momentum

remains conserved during the absorption and emission. On the other hand in the indirect band gap semiconductor,  $\mathbf{K}$  value of CBM is shifted relative to VBM, so the direct transition is not allowed here. So in this case when photon energy is higher than indirect band gap is provided, a direct transition is observed in higher energy level of conduction band and from there simultaneously via phonon emission electron relaxes to CBM. Phonon has negligible energy but very high momentum so phonon emission accounts for the momentum mismatch. Again due to momentum mismatch emission is forbidden and radiative emission is highly unlikely. That is the reason in an indirect band gap semiconductor non-radiative decay dominates the emission.

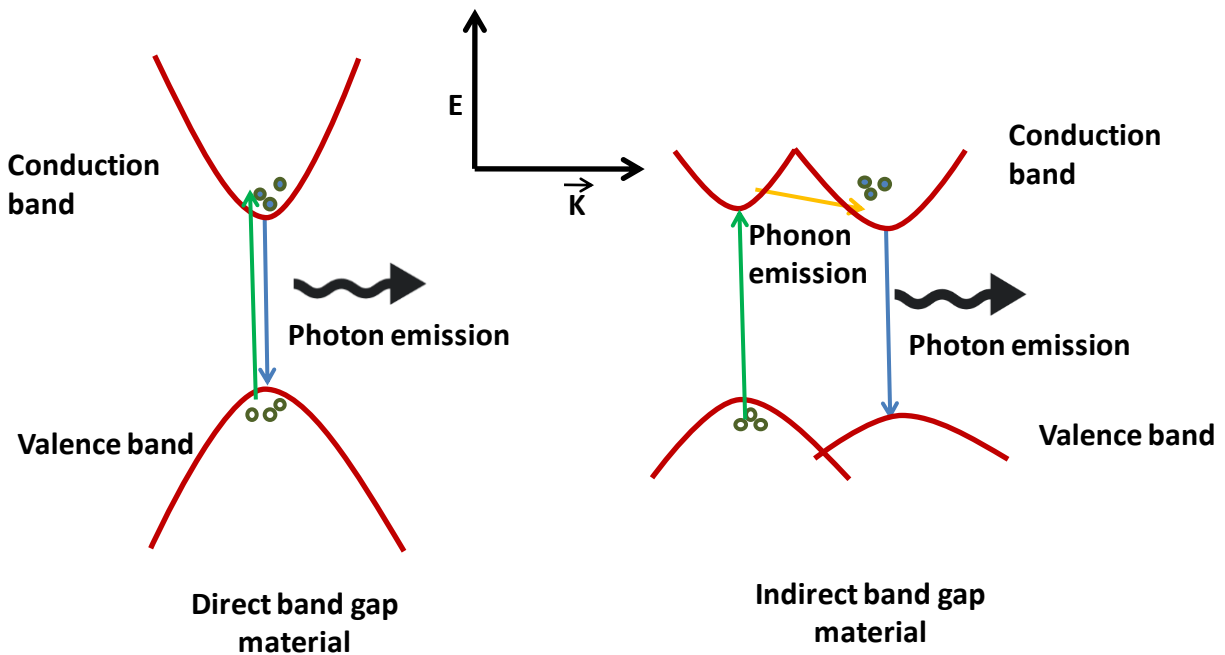


**Figure 7:** Schematic representation of electronic band structure of direct band gap semiconductor and indirect band gap semiconductor. (Figure is adapted from Greg Sun<sup>37</sup>)

One of the possible solutions to overcome this problem is by using a nanostructure of this material. When the size of a crystal becomes comparable or less than the size of the exciton Bohr radius quantum confinement effects start to play a role. Quantum confinement helps in relaxation of the momentum conservation. This can be understood through Heisenberg's uncertainty principle:

$$\Delta x \cdot \Delta p \geq h/4\pi$$



Where  $\Delta x$  and  $\Delta p$  are the uncertainties in position and momentum respectively and  $h$  is Planck constant. This formula tells that the more precisely the position of the particle is known, the less precisely its momentum can be determined and vice versa. In a bulk material, the electrons are able to move over a large distance, hence uncertainty in position is very high and therefore the momentum uncertainty is very small and for transition to take place  $\mathbf{K}$  value of both VBM and CBM has to be same. In case of NCs, the particle is well localized in a small volume (few nm) such that uncertainty in position is very less, hence the momentum uncertainty is larger than bulk. The larger uncertainty in momentum compensates the mismatch in momentum, which results in an increased relative probability of radiative recombination compared to non-radiative recombination. Since our investigation is also on the NCs, hence origin of PL can be attributed to this phenomenon as well.

#### **2.3.4 Surface characterization:**

$^1\text{H}$  NMR spectroscopy is a reliable tool to characterize presence of any organic moieties surrounding the NCs. Figure 7 shows the  $^1\text{H}$  NMR spectrum of (a)  $\text{BiI}_3$  NCs dispersed in  $\text{C}_6\text{D}_6$ , (b) oleylamine and (c) 1-octadecene. After comparing with oleylamine and 1-octadecene NMR peaks,  $\text{BiI}_3$  NCs peaks have been assigned, though the peaks at chemical shifts below 2.0 ppm values are difficult to distinguish as peaks corresponding to 1-octadecene and oleylamine shows overlapping chemical shifts in this region. Peak at 5.36 ppm corresponds to oleylamine alkene proton suggesting presence of oleylamine in the environment of  $\text{BiI}_3$  NCs. Peaks at 5 ppm and 5.8 ppm correspond to 1-octadecene suggesting presence of 1-octadecene in the environment of  $\text{BiI}_3$  NCs. Bunch of peaks around 7 ppm can be assigned to  $\text{C}_6\text{D}_6$  and anhydrous toluene (used for re-dispersion of NCs). Peak at 3.35 ppm is due to ethanol that was used in precipitating the solution of NCs. Completely dried NCs cannot be dispersed in  $\text{C}_6\text{D}_6$  hence peaks coming from toluene and ethanol are unavoidable.  $^1\text{H}$  NMR shows presence of all organic moieties and it is hard to find which one are bound and which one are not.

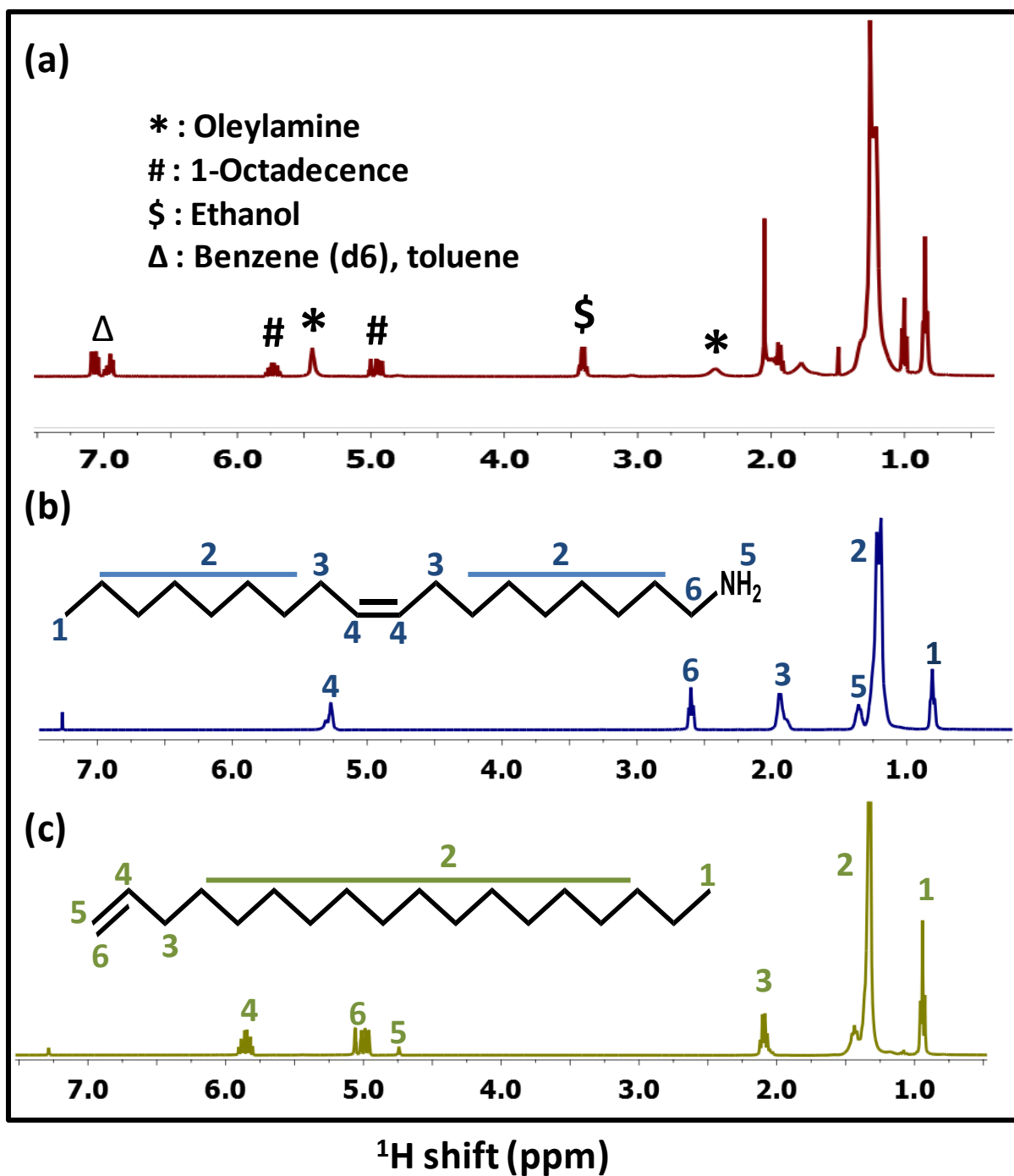


**Figure 8:**  $^1\text{H}$  NMR spectra of (a)  $\text{BiI}_3$  NCs dispersed in deuterated benzene ( $\text{C}_6\text{D}_6$ ). (b) Oleylamine. (c) 1-octadecene. Comparison of  $\text{BiI}_3$  NC spectrum with oleylamine and 1-octadecene shows presence of both in solution.

To further investigate the binding nature of capping ligands on surface of  $\text{BiI}_3$  NCs, two-dimensional diffusion-ordered spectroscopy (DOSY) was employed. Figure 8a shows

2D- DOSY spectrum of  $\text{BiI}_3$  NCs dispersed in  $\text{C}_6\text{D}_6$ . The diffusion value depends on the velocity of molecule in solution and therefore, heavier the molecule lesser the velocity and consequently smaller diffusion value. Diffusion value for 5.36 ppm (circled) which corresponds to oleylamine is minimum, so we can conclude that oleylamine is bound to NCs. However, we did not observe increased value for other oleylamine peaks; this is due to very sensitive nature of 2D-DOSY. Other than oleylamine peak we did not observe decreased diffusion value for other molecules (1-octadecene, ethanol, toluene) confirming the non-binding of those molecules. Higher diffusion values correspond to fragmented molecules.

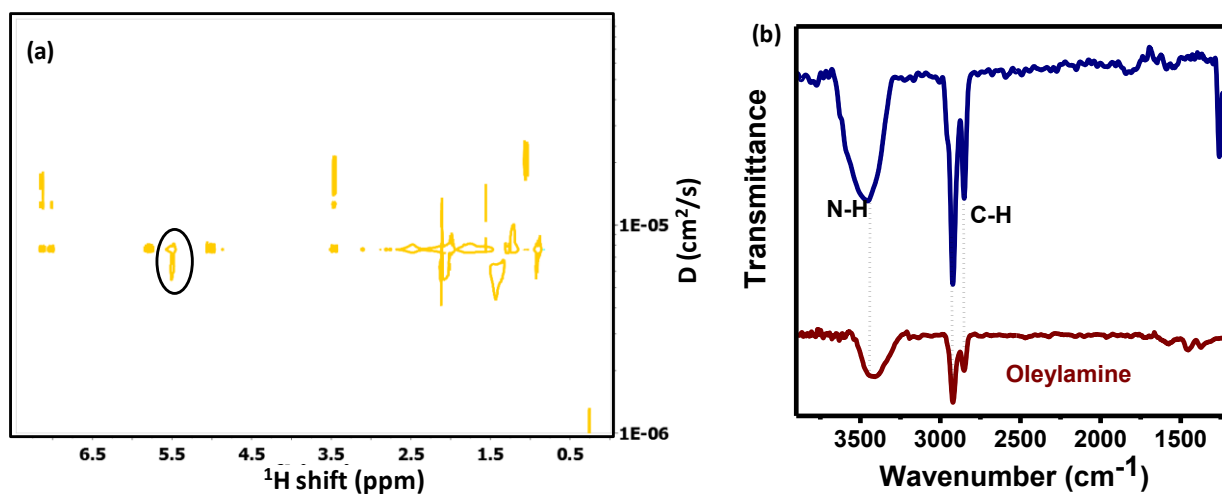


**Figure 9:** (a) DOSY spectrum of  $\text{BiI}_3$  NCs, slow diffusion corresponding to oleylamine circled in black is an evidence to claim the binding of oleylamine to NCs. (b) FTIR (Fourier transform IR) spectroscopy of  $\text{BiI}_3$  NCs plotted with free oleylamine confirms the binding of oleylamine.

Further, to support the claim of oleylamine binding FTIR spectra was measured. In figure 8b FTIR of our NCs is compared with free oleylamine. Presence of broad N-H ( $3423\text{cm}^{-1}$ ) and C-H ( $2990\text{cm}^{-1}$ ) peaks similar to reference oleylamine supports the presence of oleylamine as ligand. However, presence of 1-octadecene cannot be discarded from FTIR as it also has C-H and C=C bond. Only possible way in which 1-octadecene can bind to  $\text{Bi}^{3+}$  is through vander waal (ionic-dipole) interaction between

Bi<sup>3+</sup> and C=C, but this is very weak in nature to keep NCs dispersed in solution. Hence possibility of presence of 1-octadecene can be ruled out.

### 2.3.5 MALDI-TOF analysis:

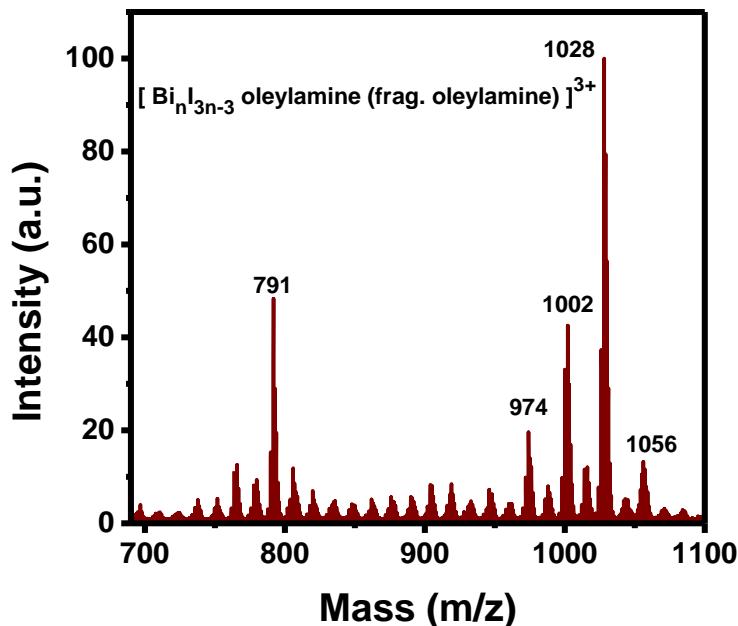


**Figure 10:** MALDI-TOF spectrum of Bi<sub>13</sub> NCs collected using dithranol matrix prepared in anhydrous chloroform.

Table 2 showing molecular formula obtained from the MALDI-TOF

M/Z	n	Formula
791	4	[Bi <sub>4</sub> I <sub>9</sub> (frag. Oleylamine)] <sup>3+</sup>
974	5	[Bi <sub>5</sub> I <sub>12</sub> (frag. Oleylamine)] <sup>3+</sup>
1002	5	[Bi <sub>5</sub> I <sub>12</sub> (frag. Oleylamine)] <sup>3+</sup>
1028	5	[Bi <sub>5</sub> I <sub>12</sub> (Oleylamine)] <sup>3+</sup>
1056	6	[Bi <sub>6</sub> I <sub>15</sub> (frag. Oleylamine)] <sup>3+</sup>

Mass spectrometry is a major technique to characterize clusters. Therefore, we measured mass spectra of small Bi<sub>13</sub> NC. Figure 10 shows MALDI-TOF spectrum of Bi<sub>13</sub>

NCs. Presence of numerous peaks suggests formation of many different sized clusters. This is the first report on mass spectrometry for  $\text{BiI}_3$  NCs or clusters, so assignments of these peaks become difficult in the absence of available standard literature. Consequently, we tried different possibilities, by taking clues from assignment of mass spectra of Au NCs in literature.<sup>34</sup> We could find a general formula  $[\text{Bi}_n\text{I}_{3n-n}(\text{fragmented oleylamine})]^{3+}$ , that can explain the major peaks in the spectrum with different values of integer “n”. Table 2 present the formula for assigned peaks. However, we cannot rule out possibility of other kind of assignment of the same spectrum. At present, the results obtained from mass spectroscopy agrees with prior characterization suggesting formation of oleylamine capped  $\text{BiI}_3$  NCs or nanoclusters.<sup>27</sup>

## 2.4. Negative Results

To obtain desired colloidal  $\text{BiI}_3$  NCs, various different synthesis strategies were employed. Before achieving already discussed  $\text{BiI}_3$  NCs, other products were also obtained. In this section we briefly discuss those results.

### 2.4.1 $\text{BiI}_3$ NCs using different synthesis scheme

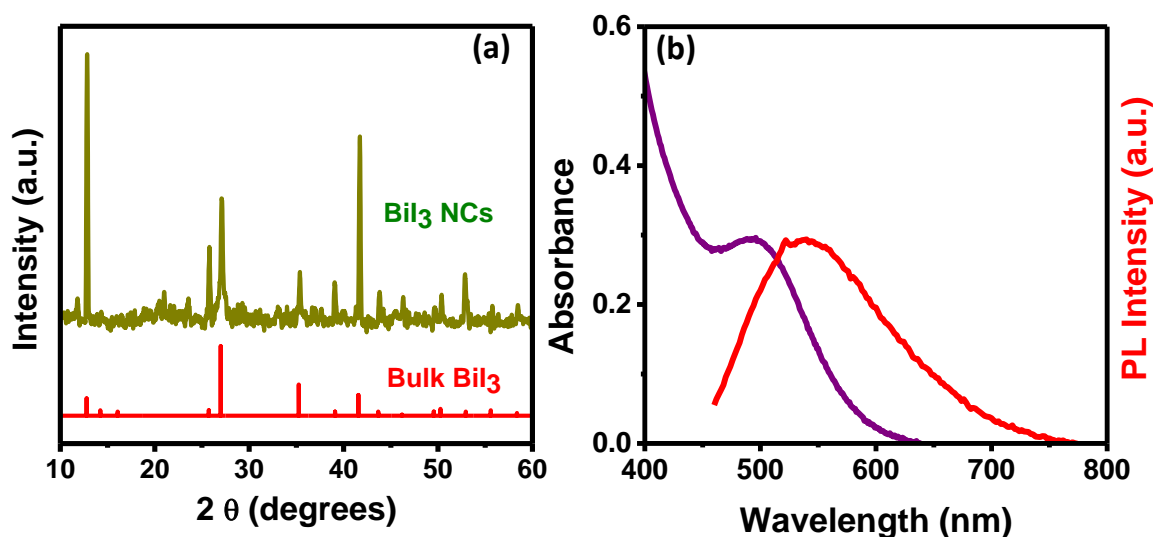


**Figure 11:** (a) p-XRD pattern of  $\text{BiI}_3$  NCs plotted with bulk  $\text{BiI}_3$ . (b) Visible absorption and PL spectra of  $\text{BiI}_3$  NCs.

This synthesis scheme employs a different route to obtain Bi precursor while maintaining rest of the procedure as described previously in experimental section. Bi precursor was made by dissolving  $\text{Bi}(\text{NO}_3)_3 \cdot 5\text{H}_2\text{O}$  in 10 ml 1-octadecene, 1 ml oleic acid at 170 °C. Figure 11a shows the p-XRD of synthesized NCs with bulk  $\text{BiI}_3$ . Whilst, most of the peaks are in agreement with bulk reference confirming the formation  $\text{BiI}_3$  NCs, we observed additional peaks that could arise as a consequence of secondary phase formation or impurities.

Figure 11b shows absorption and emission spectrum. Absorption maximum is at 498 nm which corresponds to a band gap of 2.5 eV. PL emission is centred at 539 nm with stokes shift of 40 nm (180 eV) which is a band edge emission. However, this result could not be reproduced due to poor solubility of Bi precursor.

#### 2.4.2 $\text{Bi}_2\text{O}_3$ NCs

In another reaction, Bi precursor was made by dissolving  $\text{Bi}(\text{NO}_3)_3 \cdot 5\text{H}_2\text{O}$  in 10 ml 1-octadecene, 1 ml oleylamine and 1 ml oleic acid at 200°C. p-XRD data (figure 12a) confirms the formation of  $\text{Bi}_2\text{O}_3$  NCs as all the peaks are in agreement with bulk  $\text{Bi}_2\text{O}_3$ .

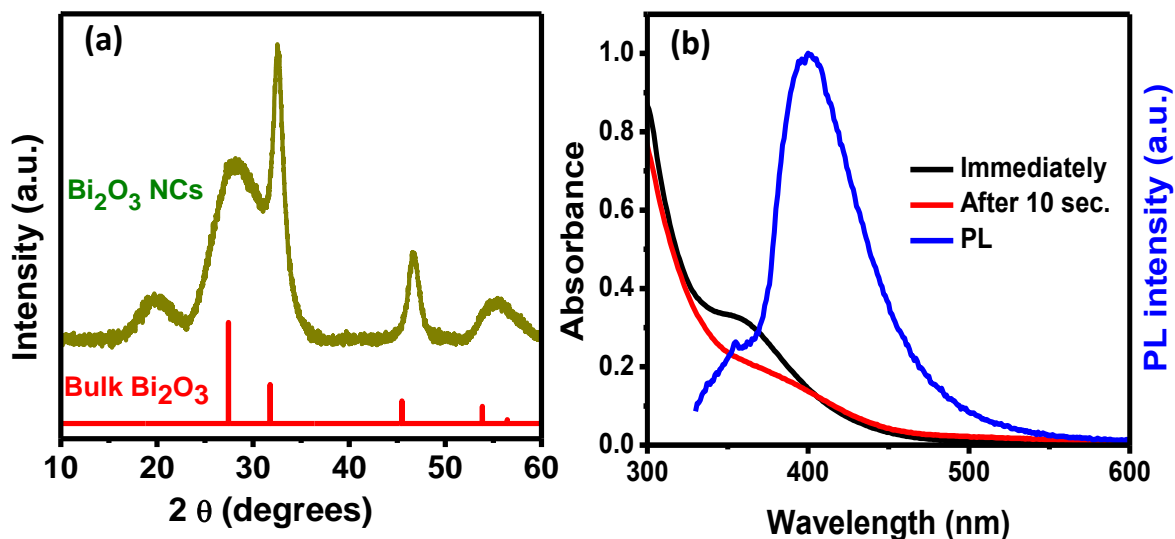


**Figure 12:** (a) p-XRD pattern of  $\text{Bi}_2\text{O}_3$  NCs plotted with bulk  $\text{Bi}_2\text{O}_3$ . (b) UV-visible absorption and PL spectra of  $\text{Bi}_2\text{O}_3$ NCs.

Figure 12b shows the UV-visible absorption and PL spectra. Absorption spectra shown for two aliquotes which were collected just after injection and another with a 10 second delay. We observe the excitonic peak at 360 nm in immediately collected aliquot which is red shifted in 10 second aliquot suggesting NC size is increasing with time. PL maximum is at 402 nm which is obtained for immediate aliquot. Extensive studies of electronic, optical properties of  $\text{Bi}_2\text{O}_3$  NCs have been done already.<sup>35</sup> So this data is just reproduction of reported literature with a different synthesis strategy.

### 2.4.3 Bi NCs

In above mention reaction  $\text{Bi}_2\text{O}_3$  NCs was collected from supernatant and when precipitate was re-dispersed in hexane and analyzed, it was found to be Bi NCs with 28 nm size. p-XRD patterns (figure 13a) are in complete agreement with Bulk Bi.

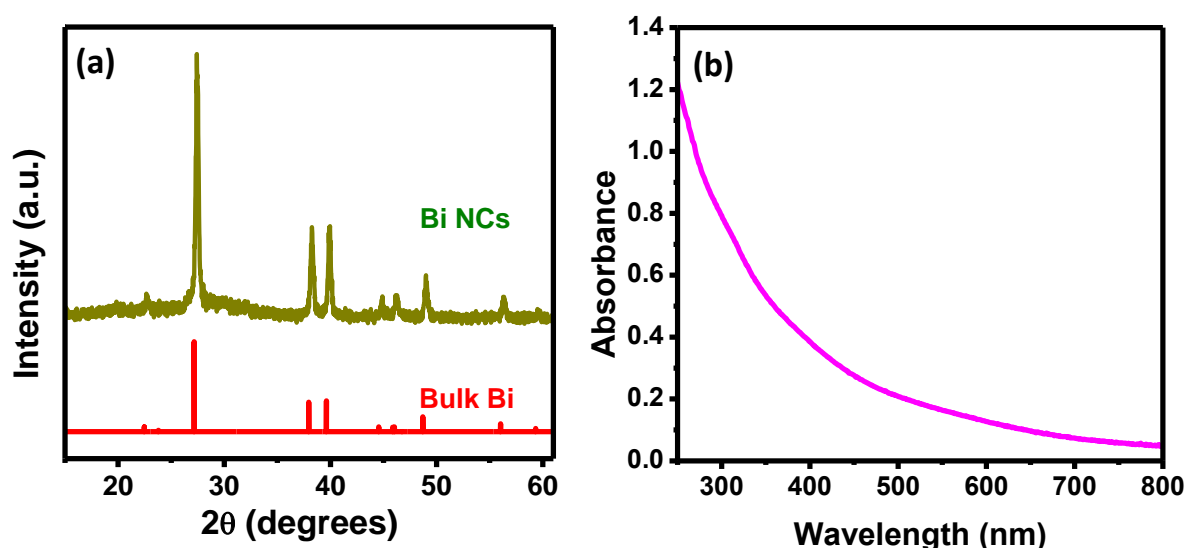


**Figure 13:** (a) p-XRD pattern of Bi NCs plotted with bulk Bi. (b) UV-visible absorption and PL spectra of Bi NCs.

Although Bi is a metal but at nano-scale it shows semi-metal behaviour with small band gap of 0.91 eV.<sup>41</sup> UV-visible absorption (figure 13b) spectrum confirms semi metal behaviour as it starts absorbing above 800nm.

## 2.5 Conclusion

We prepared  $\text{BiI}_3$  NCs and examined its fundamental optical properties. Average size of our NCs is 2.1 nm which is well below Bohr excitonic diameter.  $\text{BiI}_3$  NCs maintains excitonic absorption with band gap of 3.2 eV and excitonic emission. The  $\text{BiI}_3$  NCs exhibited 14% PLQYs, which is one of the best among all blue emitting semiconductor NCs. Radiative lifetimes of 5.9 ns and 2.4 ns were obtained. Presence of sharp escalation in band gap, high PLQY in violet region and absence of long lifetimes indicates direct band gap nature of our  $\text{BiI}_3$  NCs. Tunability could not be achieved because of highly reactive nature of Bi and I.  $\text{BiI}_3$  NCs show potential for light emitting diodes and detector owing to their low toxicity, favourable PLQY in the blue/violet spectral region. Provided the challenge to find an air-stable, nontoxic alternatives to the lead based perovskites, it is highly encouraging to explore NCs for future optoelectronic application.

Apart from this,  $\text{BiI}_3$  NCs,  $\text{Bi}_2\text{O}_3$  NCs and Bi NCs were also synthesized. But these NCs suffer from existence of impurity phase and / or poor reproducibility.



## Chapter-2

### Bulk Cs<sub>2</sub>AgBiBr<sub>6</sub> Double perovskite

#### 3.1 Introduction

In this chapter we look for a material that has similar crystal structure as of lead halide perovskite. Perovskite compounds are represented with general chemical formula ABX<sub>3</sub>, where 'A' and 'B' are two cations, and X is a halide anion. B cation octahedrally coordinates with X anion and A cation is surrounded by BX<sub>6</sub> octahedra which give rise to ideal cubic structure. The coordination number of B is 6 and A is 12. Due to bulkiness of ions, distortions are easy to occur. One of the possible solutions is to get rid of lead Pb. To find a replacement for the divalent Pb cations while maintaining charge neutrality and crystal structure one mono-valent (a<sup>1+</sup>) and one trivalent cation (b<sup>3+</sup>) is required. One of the possible choices for trivalent cation (b<sup>3+</sup>) is Bi<sup>3+</sup>. Bi<sup>3+</sup> (1 Å) have atomic radius similar to Pb<sup>2+</sup> (1.2 Å) and in addition it also possesses similar electronic band structure. For the mono-valent cations (a<sup>1+</sup>) noble metals Ag, and Au are best suited as they have similar radius to Pb<sup>2+</sup> (Ag<sup>+</sup> (1.1 Å), and Au<sup>+</sup> (1.3 Å)). Cost of Au is higher while Ag have same cost as Pb. Following this simple reasoning, in this chapter we reproduce and investigate combination of b<sup>3+</sup> = Bi and a<sup>1+</sup> = Ag.

##### 3.1.1 Crystal Structure

Cs<sub>2</sub>AgBiBr<sub>6</sub> adopts the cubic double perovskite structure with Fmmm space group. Figure 14 shows double perovskite crystal structure. Lattice parameter a is 11.2 Å<sup>15b</sup>. Within the lattice, coordinates of atoms are Ag (0, 0, 0), Cs (0.25, 0.25, 0.25), Bi (0.5, 0.5, 0.5) and Br (0.25, 0, 0).<sup>15b</sup> Similar to perovskite structure Cs<sup>+</sup> ion occupies cub-octahedral cavities in the structure. Ag<sup>+</sup> and Bi<sup>3+</sup> are octahedrally surrounded by the Br<sup>-</sup> ions. Octahedra consisting Ag<sup>+</sup> and Bi<sup>3+</sup> appear alternatively which result into a double perovskite structure. The bond distance in between Cs-Br, Ag-Br, Bi-Br are 3.985 Å, 2.822 Å, 2.813 Å,<sup>15b</sup> respectively. Br<sup>-</sup> ion is slightly shifted towards Bi<sup>3+</sup> ion due to strong

electrostatic force of attraction between two compare to  $\text{Br}^-$  and  $\text{Ag}^+$ , which leads to little shorter bond distance between Bi-Br compare to Ag-Br.

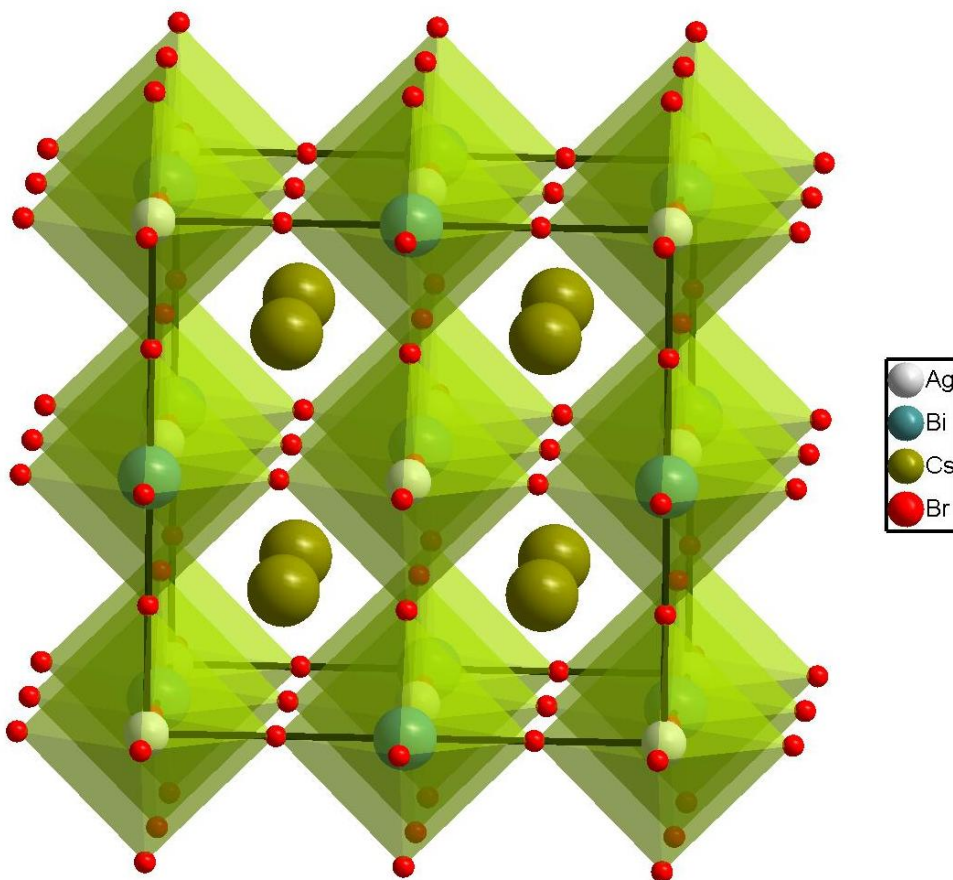


**Figure 14:** Crystal structure of  $\text{Cs}_2\text{AgBiBr}_6$ . The Cs, Ag, Bi and Br atoms are shown as green, white, blue and red spheres, respectively. Ag and Bi are at the centre of Br octahedra shown in light green polyhedral.

## 3.2 Methodology

**3.2.1 Chemicals:** Silver bromide ( $\text{AgBr}$ , purity  $\geq 98\%$ ), bismuth bromide ( $\text{BiBr}_3$ , purity  $\geq 98\%$ ), cesium bromide ( $\text{CsBr}$ , purity  $\geq 98\%$ ), hydrogen bromide ( $\text{HBr}$ , 48%), phosphoric acid ( $\text{H}_3\text{PO}_4$ , 50%) were purchased from Sigma Aldrich.

**3.2.2 Preparation:**  $\text{Cs}_2\text{AgBiBr}_6$  was prepared following the method reported previously<sup>15b</sup>. In a three necked round bottom flask a mixture of 2 mL of a 50% solution

of  $\text{H}_3\text{PO}_4$  and 8 mL 8.84 M HBr was added and heated till 135 °C under  $\text{N}_2$  atmosphere. Then, 1.41 mmol of AgBr and 1.41 mmol of  $\text{BiBr}_3$  were dissolved in the hot solution. Next, 2.82 mmol of CsBr was added to the flask. Immediately after the addition of CsBr, we observe the formation of orange coloured precipitate. Solution was centrifuged at 3000 rpm for 1 min. Precipitate was collected and washed 3 times using ethanol and dried overnight under vacuum.

### **3.3 Results and Discussion**

#### **3.3.1 Structural, morphological and elemental analysis**

Figure 15a shows the p-XRD data of synthesized  $\text{Cs}_2\text{AgBiBr}_6$  plotted with reference for bulk  $\text{Cs}_2\text{AgBiBr}_6$ . All peaks are in agreement with reference data that clearly indicates the formation of  $\text{Cs}_2\text{AgBiBr}_6$ . Since there is no additional peak, it guarantees that there is no impurity present. Sharpness of peaks indicates the formation of large size of the crystallite. Figure 15b shows SEM image of synthesized  $\text{Cs}_2\text{AgBiBr}_6$ . It shows that different kind of shape are there in system i.e. cubic, triangular, oval etc and also confirms formation of bulk size which is in agreement with p-XRD data. Elemental analysis was carried out using EDS (figure 15c), which has been tabulated in table 3. The elemental ratio is in complete agreement with the molecular formula which confirms the formation of double perovskite  $\text{Cs}_2\text{AgBiBr}_6$ .

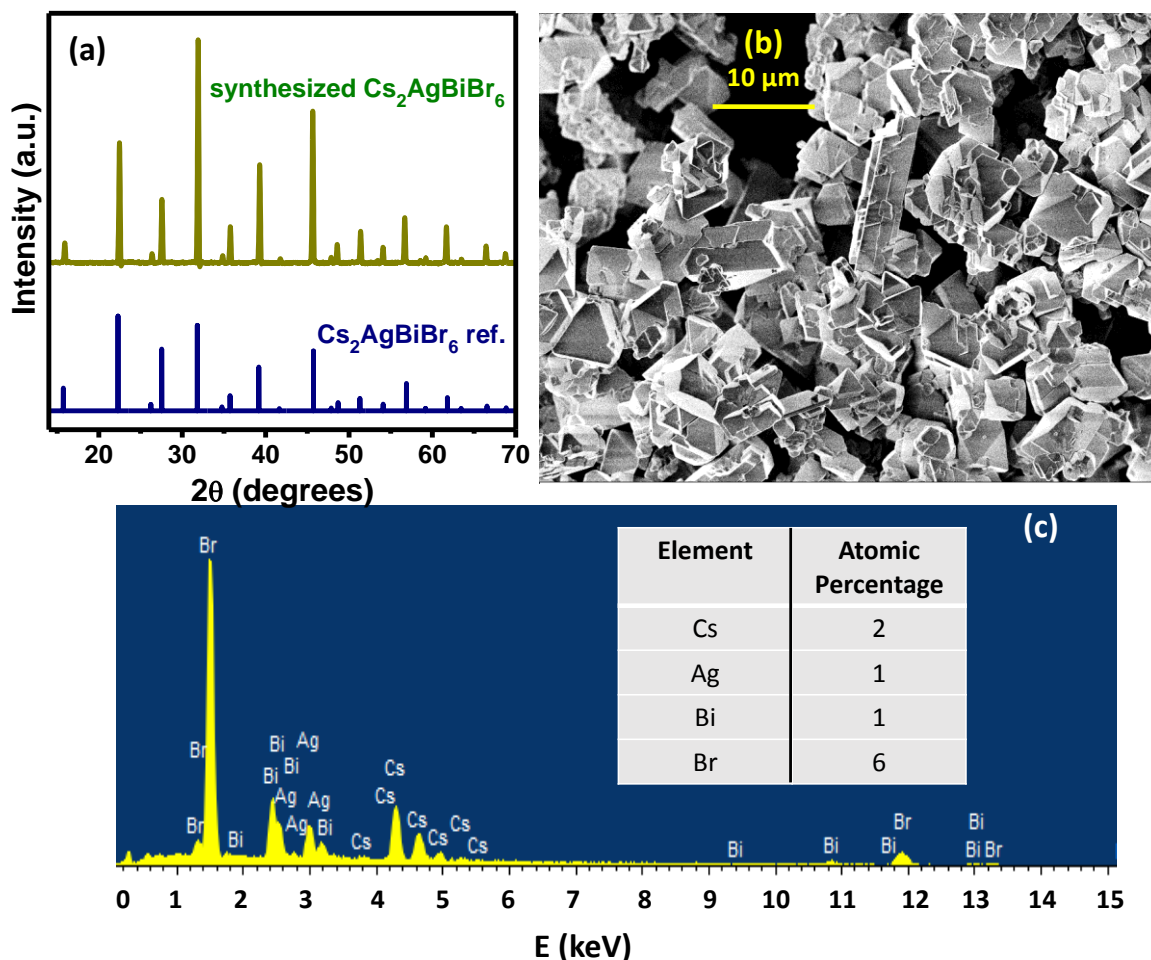


**Figure 15:** Structural, morphological and elemental characterization. (a) p-XRD spectrum of  $\text{Cs}_2\text{AgBiBr}_6$  plotted with reference  $\text{Cs}_2\text{AgBiBr}_6$ . Agreement of all peaks with reference suggest the formation of  $\text{Cs}_2\text{AgBiBr}_6$ . (b) Field Emission Scanning Electron Microscope (FESEM) image showing spherical particle with average particle diameter of 55 nm. (C) EDS spectrum shows the presence of element Cs,Ag,Bi,Br in 2:1:1:6 ratio confirms the formation of  $\text{Cs}_2\text{AgBiBr}_6$ .

### 3.3.2 Optical Characterization:

The optical band gap was determined using UV-vis diffuse reflectance spectra (Figure 16a). We observe that above 500 nm all the light is reflected back (100 %) suggesting no absorption and below that 0 reflectance indicates complete absorption of light.

However, we do not observe sharp escalation at 500 nm. Band structure calculation done by Eric et al<sup>19b</sup> attributes this phenomenon to the indirect nature of the double perovskites.

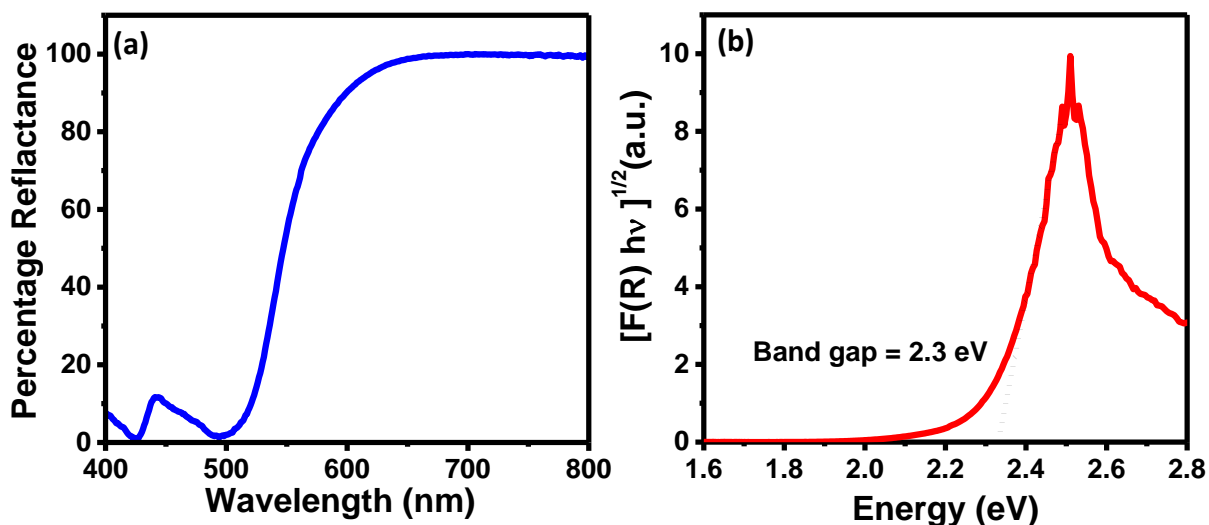


**Figure 16:** Optical characterization. (a) Diffuse reflectance spectra for Cs<sub>2</sub>AgBiBr<sub>6</sub>. (c) Tau plot showing optical band gap of 2.3 eV.

To get the optical band gap value, absorption data were obtained from UV-visible reflectance data using Kubelka-Munk equation. In the Kubelka-Munk equation absorbance is expressed in terms of reflectance through the equation:  $F(R) = \alpha = (1 - R)^2 / (2R)$ , where  $\alpha$  is the optical absorption coefficient and  $R$  is the reflectance. From the absorption data Tauc plot is obtained. Tauc plot is a plot between  $[F(R)hv]^{1/n}$  ( $\alpha$ ) and  $hv$ , where  $n$  is equal to  $1/2$  for direct band gap semiconductor and  $2$  for indirect band gap semiconductor. X-axis intercept at  $Y = 0$  gives the band gap value. Using this plot obtained band gap was 2.2 eV.

### 3.4 Conclusions

Cs<sub>2</sub>AgBiBr<sub>6</sub> double perovskite was successfully reproduced with optical gap of 2.2 eV. Optical band gap similar to CsPbBr<sub>3</sub> (2.25 eV)<sup>36</sup> demonstrate that double perovskite Cs<sub>2</sub>AgBiBr<sub>6</sub> is a promising material that can very well replace lead halide perovskites. Its

stability study is in progress. Its photo-physical application will be investigated in future studies. We are also planning to explore the synthesis through other synthetic routes and optoelectronic applications of double perovskites NCs.

#### 4. References:

1. Protesescu, L.; Yakunin, S.; Bodnarchuk, M. I.; Krieg, F.; Caputo, R.; Hendon, C. H.; Yang, R. X.; Walsh, A.; Kovalenko, M. V., Nanocrystals of Cesium Lead Halide Perovskites (CsPbX<sub>3</sub>, X = Cl, Br, and I): Novel Optoelectronic Materials Showing Bright Emission with Wide Color Gamut. *Nano Lett.* **2015**, *15*, 3692-3696.
2. Yettapu, G. R.; Talukdar, D.; Sarkar, S.; Swarnkar, A.; Nag, A.; Ghosh, P.; Mandal, P., Terahertz Conductivity within Colloidal CsPbBr<sub>3</sub> Perovskite Nanocrystals: Remarkably High Carrier Mobilities and Large Diffusion Lengths. *Nano Lett.* **2016**, *16*, 4838-4848.
3. (a) Green, M. A.; Ho-Baillie, A.; Snaith, H. J., The emergence of perovskite solar cells. *Nature Photonics* **2014**, *8*, 506-514; (b) Liu, M.; Johnston, M. B.; Snaith, H. J., Efficient planar heterojunction perovskite solar cells by vapour deposition. *Nature* **2013**, *501*, 395-398; (c) Swarnkar, A.; Marshall, A. R.; Sanhira, E. M.; Chernomordik, B. D.; Moore, D. T.; Christians, J. A.; Chakrabarti, T.; Luther, J. M., Quantum dot-induced phase stabilization of  $\alpha$ -CsPbI<sub>3</sub> perovskite for high-efficiency photovoltaics. *Science* **2016**, *354* (6308), 92-95.
4. Kang, J.; Wang, L.-W., High Defect Tolerance in Lead Halide Perovskite CsPbBr<sub>3</sub>. *J. Phys. Chem. Lett.* **2017**, *8*, 489-493.
5. Eriksson, O.; Wills, J.; Mumford, P.; Cahay, M.; Friz, W., Electronic structure of the LaS surface and LaS/CdS interface. *Phy. Rev. B* **1998**, *57*, 4067-4072.
6. Yuan, Y.; Xu, R.; Xu, H.-T.; Hong, F.; Xu, F.; Wang, L.-J., Nature of the band gap of halide perovskites ABX<sub>3</sub> (A = CH<sub>3</sub>NH<sub>3</sub>, Cs; B = Sn, Pb; X = Cl, Br, I): First-principles calculations. *Chinese Physics B* **2015**, *24*, 116302.
7. ten Brinck, S.; Infante, I., Surface Termination, Morphology, and Bright Photoluminescence of Cesium Lead Halide Perovskite Nanocrystals. *ACS Energy Lett.* **2016**, *1*, 1266-1272.
8. Manser, J. S.; Saidaminov, M. I.; Christians, J. A.; Bakr, O. M.; Kamat, P. V., Making and Breaking of Lead Halide Perovskites. *Acc. Chem. Res.* **2016**, *49*, 330-338.
9. Hoke, E. T.; Slotcavage, D. J.; Dohner, E. R.; Bowring, A. R.; Karunadasa, H. I.; McGehee, M. D., Reversible photo-induced trap formation in mixed-halide hybrid perovskites for photovoltaics. *Chem. Sci.* **2015**, *6*, 613-617.
10. (a) Eames, C.; Frost, J. M.; Barnes, P. R. F.; O'Regan, B. C.; Walsh, A.; Islam, M. S., Ionic transport in hybrid lead iodide perovskite solar cells. *Nature Communications* **2015**, *6*, 7497; (b) Meloni, S.; Moehl, T.; Tress, W.; Franckevičius, M.; Saliba, M.; Lee, Y. H.; Gao, P.; Nazeeruddin, M. K.; Zakeeruddin, S. M.; Rothlisberger, U.; Graetzel, M., Ionic polarization-induced current-voltage hysteresis in CH<sub>3</sub>NH<sub>3</sub>PbX<sub>3</sub> perovskite solar cells. *Nature Commun.* **2016**, *7*, 10334.
11. (a) Espinosa, N.; Serrano-Luján, L.; Urbina, A.; Krebs, F. C., Solution and vapour deposited lead perovskite solar cells: Ecotoxicity from a life cycle assessment perspective. *Sol. Energ. Mat. Sol. Cells* **2015**, *137*, 303-310; (b) Babayigit, A.; Duy Thanh, D.; Ethirajan, A.; Manca, J.; Muller, M.; Boyen, H.-G.; Conings, B., Assessing the toxicity of Pb- and Sn-based perovskite solar cells in model organism *Danio rerio*. *Sci. Rep.* **2016**, *6*, 18721.

12. Brandt, R. E.; Stevanović, V.; Ginley, D. S.; Buonassisi, T., Identifying defect-tolerant semiconductors with high minority-carrier lifetimes: beyond hybrid lead halide perovskites. *Mrs Commun.* **2015**, *5*, 265-275.
13. (a) Kumar, M. H.; Dharani, S.; Leong, W. L.; Boix, P. P.; Prabhakar, R. R.; Baikie, T.; Shi, C.; Ding, H.; Ramesh, R.; Asta, M.; Graetzel, M.; Mhaisalkar, S. G.; Mathews, N., Lead-Free Halide Perovskite Solar Cells with High Photocurrents Realized Through Vacancy Modulation. *Adv. Mater.* **2014**, *26*, 7122-7127; (b) Lee, S. J.; Shin, S. S.; Kim, Y. C.; Kim, D.; Ahn, T. K.; Noh, J. H.; Seo, J.; Seok, S. I., Fabrication of Efficient Formamidinium Tin Iodide Perovskite Solar Cells through SnF<sub>2</sub>-Pyrazine Complex. *J. Ame. Chem.Soc.* **2016**, *138* (12), 3974-3977.
14. (a) Pazoki, M.; Johansson, M. B.; Zhu, H.; Broqvist, P.; Edvinsson, T.; Boschloo, G.; Johansson, E. M. J., Bismuth Iodide Perovskite Materials for Solar Cell Applications: Electronic Structure, Optical Transitions, and Directional Charge Transport. *J. Phys. Chem. C* **2016**, *120*, 29039-29046; (b) Kulkarni, A.; Singh, T.; Ikegami, M.; Miyasaka, T., Photovoltaic enhancement of bismuth halide hybrid perovskite by N-methyl pyrrolidone-assisted morphology conversion. *RSC Adv.* **2017**, *7*, 9456-9460; (c) Liu, C.; Fan, J.; Li, H.; Zhang, C.; Mai, Y., Highly Efficient Perovskite Solar Cells with Substantial Reduction of Lead Content. *Sci. Rep.* **2016**, *6*, 35705.
15. (a) Slavney, A. H.; Hu, T.; Lindenberg, A. M.; Karunadasa, H. I., A Bismuth-Halide Double Perovskite with Long Carrier Recombination Lifetime for Photovoltaic Applications. *J. Ame. Chem.Soc.* **2016**, *138*, 2138-2141; (b) McClure, E. T.; Ball, M. R.; Windl, W.; Woodward, P. M., Cs<sub>2</sub>AgBiX<sub>6</sub> (X = Br, Cl): New Visible Light Absorbing, Lead-Free Halide Perovskite Semiconductors. *Chem. Mater.* **2016**, *28*, 1348-1354; (c) Volonakis, G.; Haghhighirad, A. A.; Milot, R. L.; Sio, W. H.; Filip, M. R.; Wenger, B.; Johnston, M. B.; Herz, L. M.; Snaith, H. J.; Giustino, F., Cs<sub>2</sub>InAgCl<sub>6</sub>: A New Lead-Free Halide Double Perovskite with Direct Band Gap. *J. Phys. Chem. Lett.* **2017**, *8*, 772-778.
16. Garg, A.; Tomar, M.; Gupta, V., Synthesis and Characterisation of Thin Films of Bismuth Triiodide for Semiconductor Radiation Detectors. *Conference Papers in Science* **2014**, *2014*, 3.
17. (a) Aguiar, I.; Kröger, S.; Fornaro, L., Bismuth tri-iodide polycrystalline films for X-ray direct and digital imagers. *Nuclear Instruments and Methods in Physics Research Section A: Accelerators, Spectrometers, Detectors and Associated Equipment* **2009**, *610*, 332-334; (b) Lintereur, A. T.; Qiu, W.; Nino, J. C.; Baciak, J., Characterization of bismuth tri-iodide single crystals for wide band-gap semiconductor radiation detectors. *Nuclear Instruments and Methods in Physics Research Section A: Accelerators, Spectrometers, Detectors and Associated Equipment* **2011**, *652*, 166-169; (c) Sellin, P. J., Thick film compound semiconductors for X-ray imaging applications. *Nuclear Instruments and Methods in Physics Research Section A: Accelerators, Spectrometers, Detectors and Associated Equipment* **2006**, *563*, 1-8.
18. Han, H.; Hong, M.; Gokhale, S. S.; Sinnott, S. B.; Jordan, K.; Baciak, J. E.; Nino, J. C., Defect Engineering of BiI<sub>3</sub> Single Crystals: Enhanced Electrical and Radiation Performance for Room Temperature Gamma-Ray Detection. *J. Phys. Chem. C* **2014**, *118*, 3244-3250.
19. Bismuth triiodide (BiI<sub>3</sub>) optical properties, dielectric constant, non-linear properties. In *Non-Tetrahedrally Bonded Elements and Binary Compounds I*, Madelung,



- O.; Rössler, U.; Schulz, M., Eds. Springer Berlin Heidelberg: Berlin, Heidelberg, 1998; pp 1-7.
20. Podraza, N. J.; Qiu, W.; Hinojosa, B. B.; Motyka, M. A.; Phillpot, S. R.; Baciak, J. E.; Trolrier-McKinstry, S.; Nino, J. C., Band gap and structure of single crystal BiI<sub>3</sub>: Resolving discrepancies in literature. *J. Appl. Phys.* **2013**, *114*, 033110.
  21. Lehner, A. J.; Wang, H.; Fabini, D. H.; Liman, C. D.; Hébert, C.-A.; Perry, E. E.; Wang, M.; Bazan, G. C.; Chabynyc, M. L.; Seshadri, R., Electronic structure and photovoltaic application of BiI<sub>3</sub>. *Appl. Phys. Lett.* **2015**, *107*, 131109.
  22. Trotter, J.; Zobel, T., The crystal structure of SbI<sub>3</sub> and BiI<sub>3</sub>. In *Zeitschrift für Kristallographie - Crystalline Materials*, 1966; Vol. 123, p 67.
  23. Ma, F.; Zhou, M.; Jiao, Y.; Gao, G.; Gu, Y.; Bilic, A.; Chen, Z.; Du, A., Single Layer Bismuth Iodide: Computational Exploration of Structural, Electrical, Mechanical and Optical Properties. *Sci. Rep.* **2015**, *5*, 17558.
  24. Komatsu, T.; Karasawa, T.; Akai, I.; Iida, T., Optical properties of nanostructures in layered metal tri-iodide crystals. *J. Lumin.* **1996**, *70*, 448-467.
  25. Brandt, R. E.; Kurchin, R. C.; Hoye, R. L. Z.; Poindexter, J. R.; Wilson, M. W. B.; Sulekar, S.; Lenahan, F.; Yen, P. X. T.; Stevanović, V.; Nino, J. C.; Bawendi, M. G.; Buonassisi, T., Investigation of Bismuth Triiodide (BiI<sub>3</sub>) for Photovoltaic Applications. *J. Phys. Chem. Lett.* **2015**, *6*, 4297-4302.
  26. Fornaro, L.; Aguiar, I.; Pérez Barthaburu, M.; Pereira, H. B., Synthesis of mercuric iodide and bismuth tri-iodide nanoparticles for heavy metal iodide films nucleation. *Crys. Res. Tech.* **2011**, *46*, 1317-1322.
  27. Micic, O. I.; Li, Z.; Mills, G.; Sullivan, J. C.; Meisel, D., Formation of small particles of lead iodide, mercuric iodide, and bismuth iodide layered semiconductors. *J. Phys. Chem.* **1987**, *91*, 6221-6229.
  28. Boles, M. A.; Ling, D.; Hyeon, T.; Talapin, D. V., The surface science of nanocrystals. *Nat Mater* **2016**, *15*, 141-153.
  29. Kalyuzhny, G.; Murray, R. W., Ligand Effects on Optical Properties of CdSe Nanocrystals. *J. Phys. Chem. B* **2005**, *109*, 7012-7021.
  30. Sengupta, A.; Mandal, K. C.; Zhang, J. Z., Ultrafast Electronic Relaxation Dynamics in Layered Iodide Semiconductors: A Comparative Study of Colloidal BiI<sub>3</sub> and PbI<sub>2</sub> Nanoparticles. *J. Phys. Chem. B* **2000**, *104*, 9396-9403.
  31. Sandroff, C.; Kely, S.; Hwang, D., Clusters in solution: Growth and optical properties of layered semiconductors with hexagonal and honeycombed structures. *J. Chem. Phys.* **1986**, *85* (9), 5337-5340.
  32. Boopathi, K. M.; Raman, S.; Mohanraman, R.; Chou, F.-C.; Chen, Y.-Y.; Lee, C.-H.; Chang, F.-C.; Chu, C.-W., Solution-processable bismuth iodide nanosheets as hole transport layers for organic solar cells. *Sol. Energ. Mat. Sol. Cells* **2014**, *121*, 35-41.
  33. (a) Halpern, J.; Nathans, R.; Mann, A. K., Photon Absorption Cross Sections in Bismuth and Tantalum. *Physical Review* **1952**, *88* (3), 679-680; (b) Saiz-Lopez, A.; Saunders, R. W.; Joseph, D. M.; Ashworth, S. H.; Plane, J. M. C., Absolute absorption cross-section and photolysis rate of I<sub>2</sub>. *Atmos. Chem. Phys.* **2004**, *4*, 1443-1450.
  34. Chen, T.-H.; Yu, C.-J.; Tseng, W.-L., Sinapinic acid-directed synthesis of gold nanoclusters and their application to quantitative matrix-assisted laser desorption/ionization mass spectrometry. *Nanoscale* **2014**, *6*, 1347-1353.

35. (a) Ascencio Aguirre, F. M.; Herrera Becerra, R., New synthesis of bismuth oxide nanoparticles Bi<sub>2</sub>O<sub>3</sub> assisted by tannic acid. *Appl. Phys. A* **2015**, *119*, 909-915; (b) Guo, W.; Chen, Z.; Yang, C.; Neumann, T.; Kubel, C.; Wenzel, W.; Welle, A.; Pfleging, W.; Shekhah, O.; Woll, C.; Redel, E., Bi<sub>2</sub>O<sub>3</sub> nanoparticles encapsulated in surface mounted metal-organic framework thin films. *Nanoscale* **2016**, *8*, 6468-6472; (c) Huang, X.; Zhang, W.; Tan, Y.; Wu, J.; Gao, Y.; Tang, B., Facile synthesis of rod-like Bi<sub>2</sub>O<sub>3</sub> nanoparticles as an electrode material for pseudocapacitors. *Ceramics International* **2016**, *42* (1, Part B), 2099-2105; (d) Li, W., Facile synthesis of monodisperse Bi<sub>2</sub>O<sub>3</sub> nanoparticles. *Mater. Chem. Phys.* **2006**, *99*, 174-180.
36. Stoumpos, C. C.; Malliakas, C. D.; Peters, J. A.; Liu, Z.; Sebastian, M.; Im, J.; Chasapis, T. C.; Wibowo, A. C.; Chung, D. Y.; Freeman, A. J.; Wessels, B. W.; Kanatzidis, M. G., Crystal Growth of the Perovskite Semiconductor CsPbBr<sub>3</sub>: A New Material for High-Energy Radiation Detection. *Crystal Growth & Design* **2013**, *13*, 2722-2727.